Two-Coordinate Coinage Metal Complexes as Solar Photosensitizers

Collin N. Muniz,[†] Claire A. Archer,[†] Jack S. Applebaum, Jonas Schaab, Peter I. Djurovich, Mark E. Thompson[*]

Department of Chemistry, University of Southern California, Los Angeles, CA 90089

Abstract

Generating sustainable fuel from sunlight plays an important role in meeting the energy demands of the modern age. Here we report the synthesis of new two-coordinate, molecular Cu(I) and Au(I) complexes that were designed to absorb visible photons ($\varepsilon_{vis} > 10^3$ $M^{-1}cm^{-1}$), maintain long excited state lifetimes (τ~1-0.1μs), and perform stable photo-induced charge transfer to a target substrate with remarkably potent photoreducing capabilities ($E^{+/}$* up to -2.33 V vs. $Fc^{+/0}$). The photoredox performance was evaluated in a variety of solvents, and we were able to understand the influence of ligand design and metal center on the photophysical properties. Interestingly, we found that the Cu(I) systems have competitive figures of merit with widely used scarce metal photosensitizers such as $Ru(bpy)_3^{2+}$ and $Ir(ppy)_3$. This work illuminates two-coordinate coinage metal complexes as promising, abundant metal, solar fuels photosensitizers that offer exceptional tunability and photoredox properties.

Introduction

Solar photocatalysis to generate fuel is a highly active research fields in modern chemistry.[1, 2] Molecular light-driven chemistry requires two primary processes: light absorption and chemical interaction with the substrate of interest. These tasks are often divided between two different molecules. Light absorption occurs at the photosensitizer (PS), which transfers charge onto an electrocatalyst that performs the chemical transformation. Photosensitizers such as $Ru(bpy)_3^{2+}$ and $Ir(ppy)_3$ are commonly used sensitizers due to their high stability in oxidized and reduced forms, good molar absorptivity (ε ~10^4 $M^{-1}cm^{-1}$), long-lived excited states, and the ability to efficiently deliver charge to a variety of electrocatalysts or substrates from their excited state.[3, 4] The main drawback of Ru/Ir systems is that they are among the rarest metals on earth, which precludes their use in scalable and sustainable energy technology.[5]

Chemists have responded to the challenge of developing sustainable solutions by exploring metal complexes of earth abundant metals as viable alternatives. Significant efforts have been put into first row transition metals, among which copper has been a rising candidate to match the performance of scarce metals.[6-8] The few reported copper photosensitizers have exclusively exhibited a four-coordinate structure. The most prominent classes are $Cu(I)(N\hat{}N)_2$ or $Cu(I)(N\hat{}N)(P\hat{}P)$ complexes where $N\hat{}N$ is a bisimine ligand, such as a phenanthroline or bipyridine derivative, and $P\hat{}P$ = is a bisphosphine derivative, which were pioneered by the McMillin group.[9-11] These systems exhibit a metal to ligand charge-transfer (MLCT) lowest energy excited state, and many of these four-coordinate complexes have low molar absorptivity of visible photons with absorption peak maxes in the UV to blue range with $\varepsilon > 10^3\ M^{-1}cm^{-1}$, and long excited state lifetimes of 10^2-10^5 ns. Structures such as $Cu(dmp)_2^+$ and Cu(dap)(Xantphos) have even been successfully employed in precious metal-free photoredox catalysis.[8, 10, 12-16] The challenge of controlling the absorption energy of an MLCT excited state is the restricted tunability of the metal center; energetic tuning is predominantly restricted to tuning the ligand.

Two-coordinate Cu(I) complexes have recently been investigated for applications in organic LEDs, but have never been directly investigated for solar photoredox.[17-27] It is valid to question whether or not two-coordinate complexes would work at all. These molecules are coordinatively unsaturated, which could allow for deleterious non-radiative decay of the excited state via solvent coordination. Solvent coordination and exciplex formation is a well-documented issue, even for the relatively more protected four-coordinate structures. that results in a decrease of excited state lifetime.[28] In this work, we probe the ground state photophysics and excited state photoredox capabilities in a variety of solvents to thoroughly evaluate these complexes as a new class of Cu(I) photosensitizers. We introduce three new carbene-metal-amide (cMa) complexes equipped with a mono-amido carbene (MAC) and 3,6-disubstituted carbazole (Cz) ligands shown in Figure 1. In this study, we keep the carbene ligand constant which allows us to independently investigate the role of the metal and amide ligand.

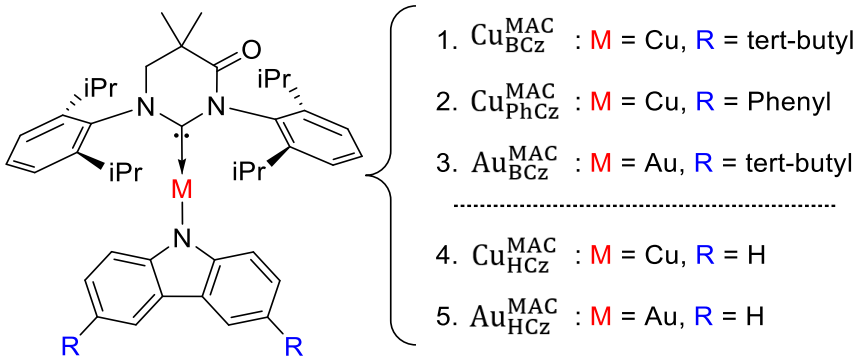

Figure 1. Structure of the three photosensitizers investigated in this work: M^{MAC}_{RCz}[M = Cu or Au, R = tert-butyl (B) or phenyl (Ph)] (iPr = isopropyl). M^{MAC}_{HCz} were reported previously and were used for comparison in this study.[21]

The lowest energy absorption of cMa complexes is typically an interligand charge transfer (ILCT) with a hole localized on the carbazole, and an electron on the carbene. Thus, the absorption energy is easily tuned by the choice of carbene and amide, which is considerable benefit in comparison to the four-coordinate MLCT systems.[17, 20, 21, 29] The MAC carbene and carbazole ligand were chosen for the complexes studied here to ensure visible light absorption with long excited state lifetimes (τ). However, carbazole is well documented to undergo irreversible oxidation which leads to oligomerization at the 3,6 - positions.[30] We circumvented this issue by installing tert-butyl and phenyl groups in the 3,6 - positions of carbazole. The photophysical and electrochemical properties of the new cMa complexes were evaluated in several common solvents for solar fuels to provide a broad understanding of their properties. Photo-induced electron transfer from the PS to a target molecule involves quenching the excited state PS^* with a quenching molecule (Q). Stern-Volmer quenching studies were performed with a variety of quenchers with increasing difficulty of reduction to evaluate the photo-reducing capabilities of each sensitizer. A Rehm-Weller analysis was used to determine the excited state oxidation potential ($E^{+/*}$) of each photosensitizer based on the results of the Stern-Volmer experiments. The role of the metal was investigated by comparing Cu(I) and Au(I) in M^{MAC}_{BCz}, and that of the amide was probed by varying the substituent groups in Cu^{MAC}_{RCz}. Here we report a completely new system for Cu(I) photosensitizers, and the first evaluation of cMa complexes as photosensitizing agents. We find that two-coordinate cMa complexes are a viable new class of photosensitizers for solar photochemistry.

3. Experimental

Synthesis: All reactions were performed under a N_2 atmosphere using a Schlenk line. Tetrahydrofuran (THF), dichloromethane, and toluene (Tol) were dried over alumina using a solvent purification system by SG Water USA, LLC. Dimethylformamide (DMF) and acetonitrile (MeCN) were purchased as dry solvents from VWR. Precursors 1,3-bis(2,6-diisopropylphenyl)-5,5-dimethyl-4-oxo-3,4,5,6-tetrahydropyrimidin-1-ium-2-ide M(I) chloride (MAC MCl [M = Cu(I) or Au(I)]), were prepared according to literature precedent.[21] The donor precursors 3,6-di-tert-butyl-9H-carbazole and 3,6-di-phenyl-9H-carbazole were purchased from AK Scientific and Tokyo Chemical Industry respectively. Sodium tert-butoxide was purchased from Sigma Aldrich. Reference compounds Cu_{Cz}^{MAC} and Au_{Cz}^{MAC} were prepared according to literature procedures.[21] All purchased chemicals were used without further purification.

Scheme 1. Synthesis of cMa photosensitizers [R = tert-butyl (B) or phenyl (Ph)].

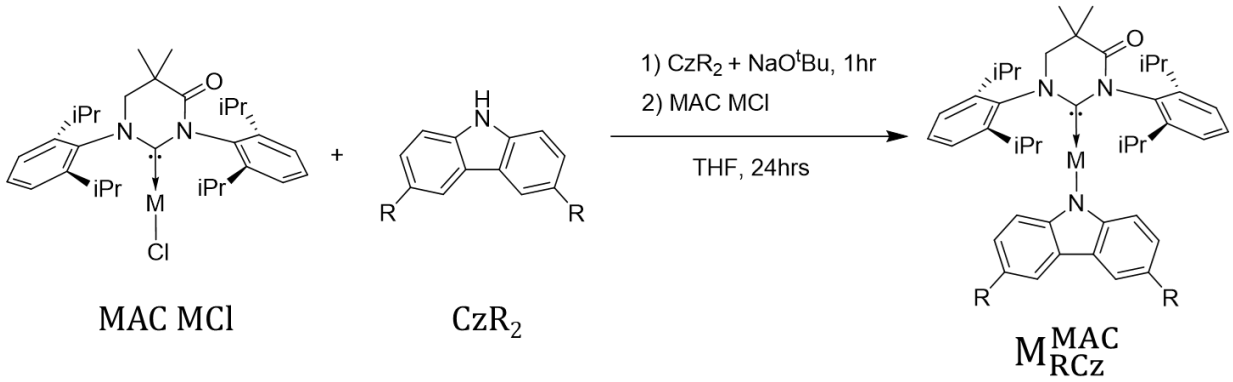

The general synthesis of all reported compounds involved adding solid CzR_2 and NaO^tBu precursors to a freshly dried Schlenk-flask connected to a Schlenk line and a nitrogen atmosphere was established. THF was added against positive N_2 pressure and the mixture stirred at room temperature for one hour to generate free carbazolide. After one hour, the MAC MCl [M = Cu or Au] complex was added against positive N_2 pressure. The flask was then covered with aluminum foil and allowed to stir at room temperature overnight. All workup was performed in air.

The workup involved filtering the reaction solution through celite and removing the solvent with a rotovap. The crude solid was dissolved in 50/50 MeCN/hexane by volume, and product was extracted into the MeCN phase. The MeCN solution was evaporated on the rotovap to yield a sticky yellow gel. The gel was redissolved in 20/80 CH_2Cl_2/hexane by volume and the solvent

removed on the rotovap, which converted the gel-like solid to a powder. The process of dissolving in 20/80 CH_2Cl_2/hexane and solvent removal was repeated three times to yield a fine yellow powder. Lastly, the solid was washed copiously with either methanol or diethyl ether to yield analytically pure samples. The detailed synthesis and analytical data for each cMa sensitizer is given in the Supporting Information (SI).

Computation: Density functional theory (DFT) and time dependent DFT (TDDFT) calculations were performed in QChem v5.0 to predict the structural and electronic properties of the cMa photosensitizers in the ground and excited states. Geometry optimizations were performed using the B3LYP method, LACVP basis, and Fit-LACVP effective core potential (ECP).[31] TDDFT calculations were performed using the LACVP basis, fit-LACVP ECP, and the CAM-B3LYP exchange (attenuation parameter = 0.2) with RPA enabled. Orbital composition analysis and wavefunction overlap of the HOMO and LUMO were evaluated using Multiwfn.[32]

Electrochemistry: Cyclic voltammetry (CV) and differential pulse voltammetry (DPV) measurements were performed with a VeraSTAT potentiostat using a glassy carbon working electrode, platinum counter electrode, and silver wire as a pseudo-reference electrode. Solutions were prepared in dry, N_2 sparged solvents with 0.1M tetrabutylammonium hexafluorophosphate electrolyte concentration. CV and DPV measurements were performed with scan rates of 0.1 Vs^{-1}, and 10mVs^{-1}, respectively. Measurements were repeated using ferrocene or decamethylferrocene as an internal standard; all measurements were referenced to the $Fc^{+/0}$ couple.

Photophysical Measurements: Absorption spectra were recorded using a Hewlett-Packard 4853 diode array spectrometer. Samples were prepared in air using either a quartz or glass cuvette. Photoluminescence (PL) spectra were recorded using a Photon Technology International QuantaMaster spectrofluorimeter. Excited state lifetime measurements were performed using time correlated single photon counting (TCSPC) with an IBH Fluorocube apparatus interfaced to a Horiba FluoroHub+ controller. Quantum yield (QY) measurements were performed using a Hamamatsu C9920 integrating sphere with a xenon lamp excitation source. Samples for PL, TCSPC, and QY measurements were prepared in a custom made long, glass cuvette that allowed the solutions to be sparged with N_2 and sealed with a Teflon valve. More information on the cuvette design is available in figure S7.

Stern-Volmer Quenching: Quenching of the excited state via photo-induced electron transfer from PS^* to Q was measured by TCSPC. Quenching via energy transfer was avoided by choosing Q such that the T_1 energy was lower than the T_1 of the PS. Five solutions were prepared with a constant photosensitizer concentration ~10 μM and increasing quencher concentration. The UV-Vis was measured to ensure that the absorption features of the PS did not change, which could indicate interaction of PS and Q in the ground state. Air-free conditions were established to prevent quenching of PS^* by oxygen. Excited state lifetimes (τ) were measured as a function of increasing quenching concentration ([Q]) and compared to the lifetime without quencher (τ_0). The Stern-Volmer equation was used to extract the rate constant k_q corresponding to quenching of the excited state.

$$\frac{\tau_0}{\tau} = 1 + k_q \tau_0 [Q] \quad (1)$$

Plots of τ_0/τ vs. [Q] yield a linear line with R^2 values near unity. For a given Stern-Volmer plot, the slope was divided by τ_0 to yield values for k_q.

4. Results and Discussion

Synthesis. The synthetic procedure shown in Scheme 1 was adapted from literature precedent.[21] The copper complexes were isolated with >63% yield, and Au_{BCz}^{MAC} was isolated with 31% yield. The final products are all indefinitely air stable as a solid. The composition was characterized by ^1H and ^{13}C NMR, CHNS elemental analysis (See SI for more details). Crystal structures were achieved through single crystal x-ray diffraction.

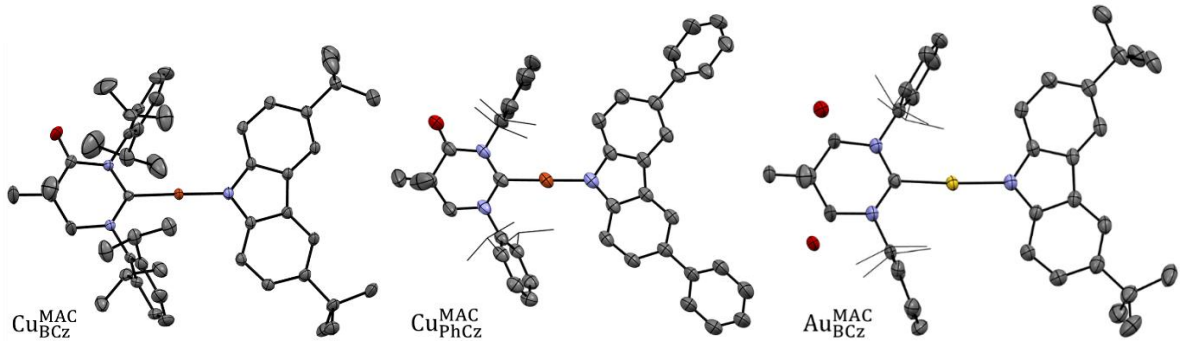

Figure 2. Single crystal structures of all new cMa complexes.

Single crystal structures of Cu_{BCz}^{MAC}, Au_{BCz}^{MAC} and Cu_{PhCz}^{MAC} reveal that the C-M-N atoms are at ~180°. All compounds have nearly coplanar ligands, with the torsion angle between the ligands varies from 6.2° to 19.6°. It has been shown that coplanar ligand orientation is important for achieving appreciable oscillator strength of the $S_0 \rightarrow S_1$ transition.[22, 23, 33] Systems with orthogonal ligands have notably low oscillator strength because the π systems of the ligand become spatially orthogonal. Au_{BCz}^{MAC} crystallized with a disorder of the C=O and the two methyl groups as shown in Figure 2.

Computational Results. The electronic structure of the ground state was examined using DFT calculations for the cMa complexes. All materials have their highest occupied molecular orbital (HOMO) localized on the carbazole, and lowest unoccupied molecular orbital (LUMO) localized on the carbene carbene. Both orbitals have a small contribution from the metal d orbital.

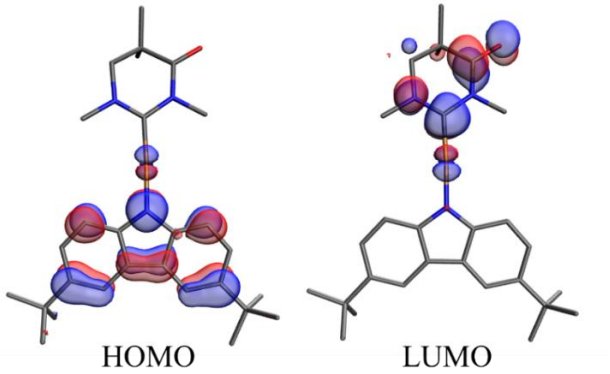

Figure 3. The HOMO and LUMO wavefunctions of Cu_{BCz}^{MAC} displayed with isovalue = 0.1. The 3,6-diisopropylphenyl groups and hydrogen atoms were omitted for clarity. The HOMO/LUMO densities of Cu_{PhCz}^{MAC} and Au_{BCz}^{MAC} are qualitatively the same and are available in Figure S1 in the SI.

Table 1 shows that the HOMO energies are selectively tuned by substitutions on the carbazole ligand, whereas the LUMO energies remain effectively constant. The LUMO energies remain constant because each reported complex has the same carbene ligand. The energy of the HOMO for the Cu analogues is destabilized in the order $Cu_{BCz}^{MAC} > Cu_{Cz}^{MAC} > Cu_{PhCz}^{MAC}$ which is consistent with the electron donating nature of the ^{t}Bu group, and electron withdrawing nature of the phenyl group. Changing the metal from Cu to Au also stabilizes the HOMO which is ascribed to the higher ionization potential of Au(I) relative to Cu(I).[34] The choice of metal ion does not

affect the LUMO energies due to the nature of the dative carbene-metal bond compared to the relatively ionic M^+-Cz^- interaction.

Table 1. Computational results of each photosensitizer. Here, *f* corresponds to the oscillator strength of the transition, and $\Lambda_{h+,e-}$ is the overlap between the hole and electron wavefunctions.

	HOMO (eV)	LUMO (eV)	$S_0 \rightarrow S_1$ (eV/*f*)	$T_1 \rightarrow S_0$ (eV)	ΔE_{ST}[a] (eV)	% metal (HO/LU)	$\Lambda_{h+,e-}$ (S_1) (%)
Cu_{BCz}^{MAC}	-4.08	-1.99	2.41/0.12	2.19	0.22	4.4/7.8	27
Cu_{Cz}^{MAC}	-4.17	-1.99	2.48/0.11	2.26	0.22	4.6/7.8	26
Cu_{PhCz}^{MAC}	-4.23	-2.08	2.51/0.14	2.32	0.19	3.3/7.8	25
Au_{BCz}^{MAC}	-4.22	-1.98	2.59/0.19	2.33	0.26	4.1/9.0	31
Au_{Cz}^{MAC}	-4.32	-1.99	2.66/0.16	2.41	0.25	4.3/9.1	36

Analysis of the excited states using TDDFT shows that the hole and electron wavefunctions in the $S_0 \rightarrow S_1$ transition is well described by the HOMO and LUMO respectively. Consequently, the energy of this interligand charge transfer (ICT) mirrors the trend in HOMO energy, since the energy of the LUMO is relatively invariant in these complexes. The energy of the T_1 state lies close in energy to the S_1 state because of the large spatial separation between the hole and electron centers of charge for two-coordinate cMa complexes. Small exchange energies and strong spin orbit coupling are known to promote rapid $T_1 \rightarrow S_1$ inter-system crossing and thermally assisted delayed fluorescence (TADF) in two-coordinate complexes with coplanar ligands. [18, 35] Comparing Cu_{BCz}^{MAC} and Cu_{Cz}^{MAC} to their gold analogues shows an increase in oscillator strength for the $S_0 \rightarrow S_1$ transition. This is consistent with the HOMO/LUMO overlap trend which suggests the Au(I) metal center induces greater orbital overlap than Cu(I). This is interesting because the metal d orbital contributes a small, albeit important point of overlap between the HOMO and LUMO. To further investigate this feature, the contribution of the metal atom in each orbital was computed using the Hirshfeld method.[32] The product of the metal orbital contribution to the HOMO and LUMO ($\%M_{HOMO} \times \%M_{LUMO}$) is higher for the gold complex (36-39%) with respect to their copper analog (26-36%). This result leads to an increase in oscillator strength for the $S_0 \rightarrow S_1$ transition in the Au derivative.

Electrochemical Results: Electrochemical measurements were performed to evaluate the ground state redox potentials and reversibility of the cationic and anionic species of the cMa complexes in a variety of solvents that are suitable for solar fuels.[36-38]

Table 2. Electrochemical potentials of cMa complexes in CH_2Cl_2, DMF, THF, and MeCN. The full CV and DPV for all table entries can be found in the SI (Figures S3 – S6).

		$E^{+/0}$ [a]	$E^{0/-}$ [a]			$E^{+/0}$ [a]	$E^{0/-}$ [a]
CH_2Cl_2	Cu_{BCz}^{MAC}	0.06	[b]	THF	Cu_{BCz}^{MAC}	0.06	-2.54
	Cu_{PhCz}^{MAC}	0.17	[b]		Cu_{PhCz}^{MAC}	0.12	-2.62
	Au_{BCz}^{MAC}	0.13	[b]		Au_{BCz}^{MAC}	0.18	-2.62
	Cu_{Cz}^{MAC}	0.19	[b]		Cu_{Cz}^{MAC}	0.18	-2.61
	Au_{Cz}^{MAC}	0.22	[b]		Au_{Cz}^{MAC}	0.28	-2.55
DMF	Cu_{BCz}^{MAC}	0.06	-2.54	MeCN	Cu_{BCz}^{MAC}	0.04	-2.51
	Cu_{PhCz}^{MAC}	0.12	-2.54		Cu_{PhCz}^{MAC}	0.13	-2.52
	Au_{BCz}^{MAC}	0.18	-2.52		Au_{BCz}^{MAC}	0.21	-2.47

[a] Potentials are in Volts vs. Fc+/0 couple, [b] Reductions are outside of the solvent window.

The redox potentials are nearly independent of solvent, however the electrochemical reversibility does depend on the solvent. The reduction is reversible for all reported cMa complexes across all solvents. Further, the reduction potentials of all are effectively the same. This is consistent with the LUMO being localized on the carbene ligand because all complexes have the same MAC carbene ligand. The trend in oxidation potentials also follows the computational trends of the HOMO. $E^{+/0}$ of Cu_{Cz}^{MAC} is greater than that of Cu_{BCz}^{MAC} and Cu_{PhCz}^{MAC} , but less than that of the Au-analog.

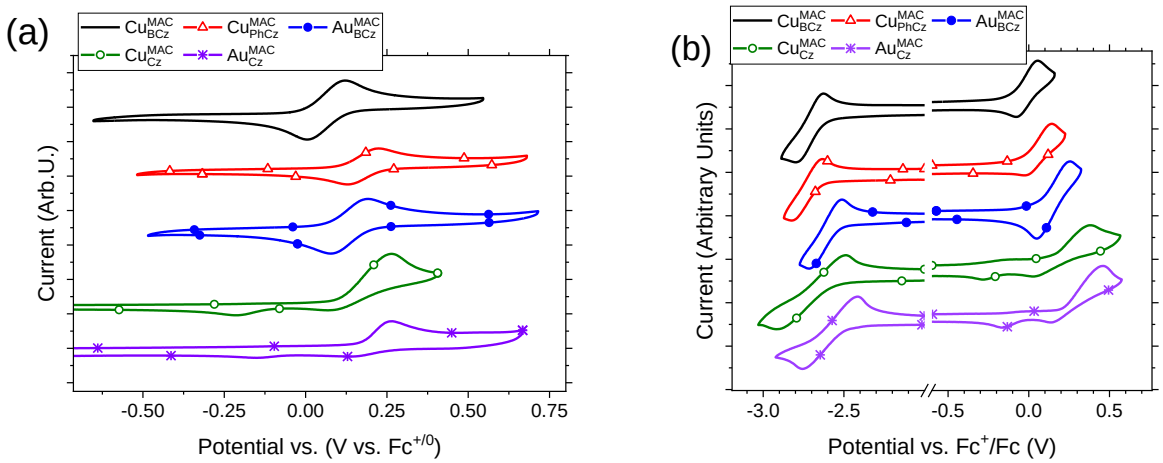

Figure 4. Cyclic voltammetry of all complexes in CH_2Cl_2 (a) and THF (b). The reduction event was outside of the solvent window for CH_2Cl_2 therefore, only the oxidative sweeps are shown here.

Cu^{MAC}_{Cz} and Au^{MAC}_{Cz} undergo irreversible oxidation in CH_2Cl_2 and THF as shown in Figure 4. The oxidation is also irreversible in DMF, and MeCN (Figures S4-S5). Irreversible oxidation is to be expected since the HOMO is localized on carbazole; a ligand which irreversibly oxidizes due to oligomerization at the 3,6-positions. The small oxidation features for these cMa complexes at ~ -0.25 V to 0.2 V only appear after the second cycle, and have been assigned to oxidation of the oligomerization products.[30] These features are not present in any of the cMa complexes with substituents on the 3,6-position of carbazole. Thus, installation of tert-butyl or phenyl groups leads to enhanced oxidative stability in CH_2Cl_2 and THF on the timescale of seconds. In MeCN (Figure S4), none of the cMa complexes undergo reversible oxidation. In DMF, however, the return wave of the first oxidation diminishes for all reported copper cMa complexes, but Au^{MAC}_{BCz} maintains a return wave. This result suggests that the oxidative stability of Au cMa complexes is greater than the Cu analogs in solution.

Photophysical Properties: The photophysical properties of the cMa complexes were examined in polar and non-polar solvents. All compounds display broad, gaussian-like absorption bands in the visible spectrum which is assigned to the $S_0 \rightarrow S_1$ ICT transition. These bands have reasonable molar absorptivity values for a charge-transfer transitions (Cu^{MAC}_{BCz}: $\varepsilon = 4x10^3$ $M^{-1}cm^{-1}$ at 435 nm, Cu^{MAC}_{PhCz}: $\varepsilon = 6x10^3$ at 425 nm, Au^{MAC}_{BCz}: $\varepsilon = 8x10^3$ $M^{-1}cm^{-1}$ at 427 nm).[39-43] The emission is shown in Figure 5b is broad and featureless with a large stokes-shift, which is typical for cMa complexes.

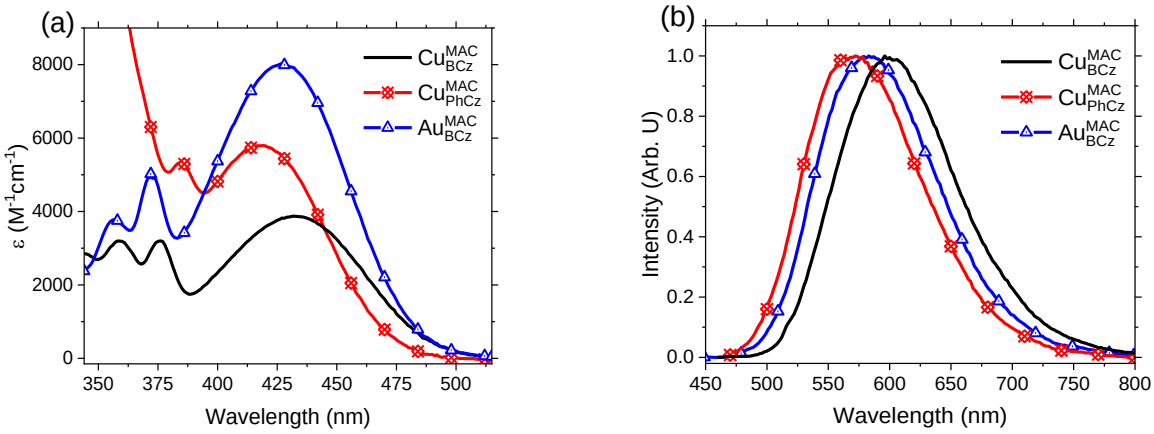

Figure 5. (a) Molar absorptivity and (b) the emission of all compounds in THF. The full spectrum from 250 nm to 550 nm is provided in Figure S6.

The blue shift in the absorption λ_{max} from Cu_{BCz}^{MAC} to Cu_{PhCz}^{MAC} and Au_{BCz}^{MAC} is due to the stabilization of the HOMO in the PhCz and Au complexes, as discussed above. The difference in molar absorptivity between Cu_{BCz}^{MAC} and Cu_{PhCz}^{MAC} also stems from the blue shift of the $S_0 \rightarrow S_1$ band which encroaches on the $S_0 \rightarrow S_2$ local excitation of 3,6-diphenylcarbazole, giving Cu_{PhCz}^{MAC} a slightly higher ε than Cu_{BCz}^{MAC}. The increased ε in Au_{BCz}^{MAC} compared to Cu_{BCz}^{MAC} is explained by the increase in oscillator strength of the $S_0 \rightarrow S_1$ absorption in Table 1.

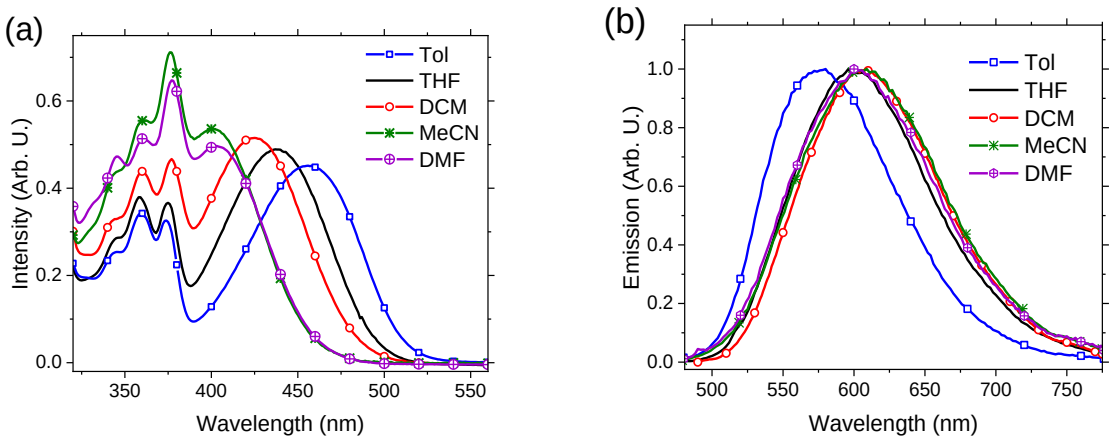

Figure 6. Solvent dependent absorption (a) and emission (b) spectra for Cu_{BCz}^{MAC}. Spectra for Cu_{PhCz}^{MAC} and Au_{BCz}^{MAC} are shown in Figures S9 and S10.

Photophysical properties were explored in solvents of varying polarity (toluene, THF, CH_2Cl_2, MeCN, and DMF, Figure 6 (a). With increasing solvent polarity the absorption band for the ICT transition blue shifts, whereas the emission red shifts. This solvatochromism has been previously explained by the large change in dipole between the ground and excited state of these molecules.[19] Here we observe that solvatochromism is markedly more pronounced in the absorption spectrum than the emission spectrum.

An important consideration for a photosensitizer is the lifetime of the excited state, which must persist long enough for the PS^* to diffuse to an electrocatalyst and transfer charge. For highly endergonic electron transfer processes, the rate constant of electron transfer (k_q) typically plateaus at ~$1x10^{10}$ $M^{-1}s^{-1}$.[44-46] Equation 1 shows that the total quenching rate also depends on the concentration of the quencher ([Q]), which would be the concentration of the electrocatalyst in a solar fuels setup. Electrocatalyst concentrations of 1-10 mM correspond to quenching rates of $1x10^7$ s^{-1} and $1x10^8$ s^{-1} respectively. These rates correspond to quenching lifetimes of 100-10ns. The excited state lifetime (τ) and quantum yield (Φ) were measured, and the radiative and non-radiative rate constants (k_r and k_{nr}) were calculated in toluene, THF, CH_2Cl_2, MeCN, and DMF in Table 3.

Table 3. Photophysical parameters in various solvents.

	solvent	λ_{max} abs (nm)	λ_{max} em (nm)	τ (ns)	Φ	k_r ($10^5 s^{-1}$)	k_{nr} ($10^5 s^{-1}$)
Cu^{MAC}_{BCz}	Toluene	455	574	720	0.34	4.7	9.2
	THF	435	603	350	0.17	4.7	24
	CH_2Cl_2	425	608	190	0.10	5.2	47
	DMF	402	607	130	0.04	3.1	74
	MeCN	403	607	120	0.04	3.4	81
Cu^{MAC}_{PhCz}	Toluene	445	556	710	0.70	9.9	4.2
	THF	424	578	460	0.43	9.4	12
	CH_2Cl_2	413	584	330	0.29	8.7	21
	DMF	393*	584	190	0.14	7.6	47
	MeCN	393*	584	190	0.16	8.4	44
Au^{MAC}_{BCz}	Toluene	449	568	450	036	8.0	14
	THF	427	584	250	0.15	6.0	34
	CH_2Cl_2	421	600	130	0.08	6.0	70
	DMF	398	598	75	0.05	6.7	130
	MeCN	400	600	69	0.04	5.8	140

* Values cannot be accurately determined because the ICT absorption band overlaps with the ligand localized transitions at higher energy.

Notably, the excited state lifetime is longer than intermolecular diffusion in all solvent systems. However, the excited state lifetime drops with solvent polarity for each photosensitizer. This decrease in lifetime is due to an increase in non-radiative decay as a function of solvent polarity (See Figure S11). Toluene yields the longest excited state lifetimes, and the most visible light absorption. The enhanced absorption of visible light due to the red shift of the ICT transition with decreasing solvent polarity. However, non-polar solvents can lead to additional kinetic barriers for intermolecular charge transfer. We opted to perform quenching studies in THF because it is polar enough to facilitate efficient electron transfer and photoredox reactions, and gives the highest

absorptivity of the polar solvents. Furthermore, THF is the only polar solvent that sustains reversible oxidation and reduction for all photosensitizers.

Photoredox Properties. Molecules in the excited state are more potent oxidizing and reducing agents than in their ground state. Redox potentials in the excited state are related to the redox potentials in the ground state and the energy gained by absorbing a photon. These potentials are related by Equations 2 and 3.[47]

$$E^{+/*} = E^{+/0} - E_{00} \quad (2)$$

$$E^{*/-} = E^{0/-} + E_{00} \quad (3)$$

where E_{00} is the energy corresponding to the midpoint between the $S_0 \rightarrow S_1$ absorption and $S_1 \rightarrow S_0$ emission. This relationship is shown graphically in Figure 7.

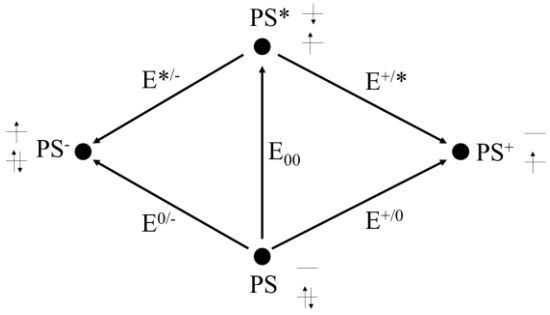

Figure 7. Latimer diagram relating the ground state photosensitizer (PS) to the excited state (PS*) through ground state and excited state redox couples, and the optical excited state energy E_{00}.

Table 4. Ground and excited state redox potentials for the cMa complexes in THF.[a]

complex	$E^{+/0}$ (V)	$E^{0/-}$ (eV)	E_{00} (eV)	$E^{+/*}$ (V)	$E^{*/-}$ (V)
Cu_{BCz}^{MAC}	0.01	-2.65	2.44	-2.43	-0.21
Cu_{PhCz}^{MAC}	0.12	-2.65	2.57	-2.45	-0.08
Au_{BCz}^{MAC}	0.13	-2.60	2.51	-2.38	-0.09

[a] Potentials are referenced to internal $Fc^{+/0}$.

Equations 2 and 3 predict that the cMa complexes are capable of being potent photo-reducing agents with near equal values of $E^{+/}*$ (-2.4 V vs. $Fc^{+/0}$), whereas they are only mild photo-oxidants. The near degeneracy of $E^{+/}*$ reflects the trend in increasing energy of E_{00} (Cu_{BCz}^{MAC} > Cu_{PhCz}^{MAC} > Au_{BCz}^{MAC}) being offset by an increase in oxidation potential for each complex. This behavior is to be expected in a system where the energy of the S_1 state is dictated by a transition involving the energy of a spatially separated HOMO and LUMO. Substituents that stabilize/destabilize the oxidation potential will stabilize/destabilize E_{00} accordingly. Thus, the value for $E^{+/}*$ is largely governed by the choice of carbene. Analogously, the value for $E^{*/-}$ is approximately governed by the choice of metal and amide donor since these moieties determine the energy of the HOMO. Photo-oxidative quenching of the cMa complexes was therefore investigated due to their remarkably high $E^{+/}*$ values.

The thermodynamic driving force of quenching an excited state via electron transfer (ΔG) depends on the values of $E^{+/}*$ of the photosensitizer $\left(E_{PS}^{+/*}\right)$, $E^{0/-}$ of the quencher $\left(E_{Q}^{0/-}\right)$, and work terms (W_s) associated with coulombic interactions of separating charge in the solvent medium (eq 4).[48]

$$\Delta G = \left(E_{PS}^{+/*} - E_{Q}^{0/-}\right) + W_s \qquad (4)$$

As the quenching molecule becomes harder to reduce, the rate of electron transfer is expected to decrease sharply when $\Delta G > 0$. The initial step for electron transfer from the excited photosensitizer (PS^*) to a quenching molecule (Q) requires the two species to diffuse together to form an encounter complex [PS*,Q] with rate constant k_d (Scheme 2). This encounter complex can relax through concomitant radiative and non-radiative processes (k_r and k_{nr}), or it can be quenched by transferring an electron or energy to the quencher. Here, we focus only on quenching via charge transfer by choosing quenchers that have energies for their S_1 and T_1 states well above those of the cMa complexes, precluding quenching by energy transfer. Electron transfer occurs with a rate constant k_{eT}, and the resultant charge separated pair [PS^+,Q^-] can either recombine by back electron transfer with rate constant k_{beT}, or to form the ground state with rate constant k_{re}. The charge separated pair can also diffuse away from each other as individual species ($PS^+ + Q^-$) with rate constant k_s.

Scheme 2. Kinetic scheme for the oxidative quenching of a photosensitizer.

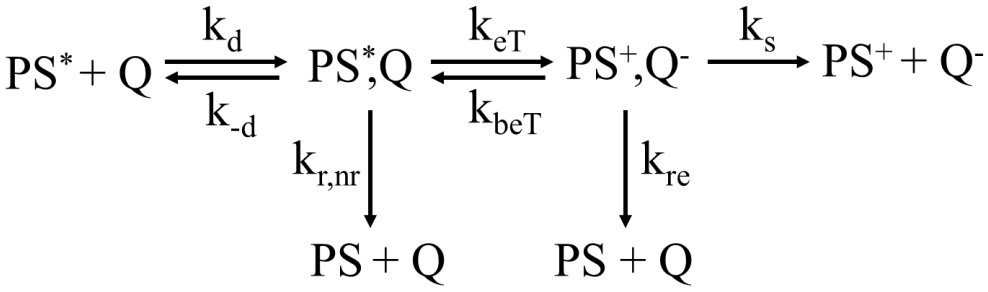

Rehm and Weller showed that the net quenching rate constant k_q given by eq 5 must consider the equilibrium which forms the encounter complex ($k_d/k_{-d} = \Delta V_{1,2}$), and charge recombination (k_{re}):

$$k_q = \frac{k_d}{1 + \left(\frac{k_d}{\Delta V_{12} \times k_{re}}\right)\left(\exp\left(\frac{\Delta G^{\ddagger}}{RT}\right) + \exp\left(\frac{\Delta G}{RT}\right)\right)} \quad (5)$$

where *R* is the ideal gas constant, T is temperature, and ΔG is given by equation 3.[49] The free energy term ($\Delta G^{\ddagger}$) accounts for the reorganization energy of (PS^*,Q) to (PS^+,Q^-) and the solvent reorganization required for electron transfer (ΔG_r).

$$\Delta G^{\ddagger} = \left[\left(\frac{\Delta G}{2}\right)^2 + (\Delta G_r)^2\right]^{\frac{1}{2}} + \frac{\Delta G}{2} \quad (6)$$

Rate constants of luminescence quenching for each complex were derived from Stern-Volmer analysis of experiments performed in THF using quenchers with varying reduction potentials; quinoxaline (QNX), N--methylpthalimide (NMeP), N,N-dimethyl-4-nitroaniline (DMNA), nitrobenzene (NB), and perinapthenone (PN). The reduction potentials for each quencher is given in Table 5 and plots of Stern-Volmer quenching data are given in the SI (Figures S12 and S13).

Table 5. Stern-Volmer quenching rate constants (k_q) for the cMa complexes measured in THF. Reduction potentials of the quenching molecules were measured using differential pulse voltammetry (Figure S2) and are reported vs. $Fc^{+/0}$.

	$E^{0/-}$ (V)	$k_q(Au_{BCz}^{MAC})$ (10^9 $M^{-1}s^{-1}$)	$k_q(Cu_{BCz}^{MAC})$ (10^9 $M^{-1}s^{-1}$)	$k_q(Cu_{PhCz}^{MAC})$ (10^9 $M^{-1}s^{-1}$)
QNX	-2.18	--	0.064	0.14
NMeP	-1.92	0.8	2.3	3.1
DMNA	-1.90	2.1	2.8	3.5
NB	-1.62	8.0	9.9	11
PN	-1.50	9.5	11	11

Analysis of the Stern-Volmer data for a given quenching molecule shows that rate of k_q is fastest for Cu_{PhCz}^{MAC} and slowest for Au_{BCz}^{MAC} (Table 5). This behavior mirrors the energy of $E^{+/}*$ for the complexes estimated using equation 2. An increase in k_q is apparent as $E^{0/-}$ becomes less negative. This change is due to an increase in the driving force of electron transfer from PS^* to Q ($\Delta G^{\ddagger}$) as the quenching molecule becomes easier to reduce. When the driving force becomes significantly large, k_q plateaus at $1.1x10^{10}$ s^{-1}, which corresponds to diffusion-limited quenching. In this regime, the slowest step in Scheme 2 is diffusion of PS^* to Q to form the encounter complex (PS^*,Q). Thus, the value for k_d in the Rehm-Weller fit was set to $1.1x10^{10}$ s^{-1}. Details for the other parameters used in the fits are given in the SI. Values of $E^{+/}*$ for each complex were determined from fits of the quenching rates to equation 5 (Figure 8). The values for $E^{+/}*$ obtained from fits to the data in Figure 8 are -2.28 V for Cu_{BCz}^{MAC}, -2.33 V for Cu_{PhCz}^{MAC}, and -2.23 V for Cu_{BCz}^{MAC}. Thus, the trend in k_q parallels the same trend in oxidation potential of the complexes (Cu_{PhCz}^{MAC} > Cu_{BCz}^{MAC} > Au_{BCz}^{MAC}). This analysis suggests that the small difference in $E^{+/}*$ values found for the three complexes is consistent with the predictions of equation 2, yet 100-170 meV lower than the estimates of -2.4 V. The disparity can be accounted for by considering that E_{00} used in equation 2 is based on the $S_0 \rightarrow S_1$ transition. Intersystem crossing is extremely rapid in the cMa complexes ($k_{ISC} > 10^9$ s^{-1}) and they are likely quenched out of the long-lived triplet excited state (T_1).[21] The energy of the T_1 state for Au_{Cz}^{MAC} was reported to be 90 meV lower than the S_1 state, which accounts for most of the difference in $E^{+/}*$.[17] A similar ΔE_{ST} value of 90 meV is expected

for the reported photosensitizers because experimental ΔE_{ST} values in cMa complexes do not vary significantly between Cu and Au complexes. Since substitutions to the amide ligand do not contribute significantly to the hole NTO, it is reasonable to assume similar ΔE_{ST} values for the two copper analogs as well.

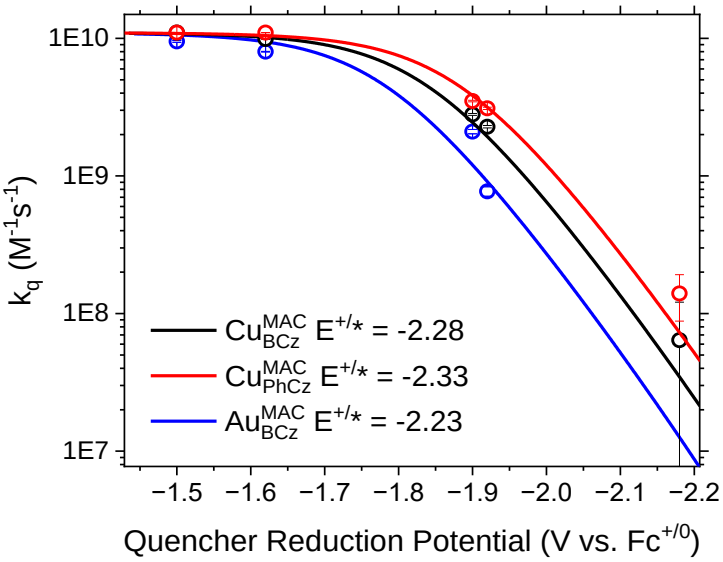

Figure 8. Rehm-Weller analysis of the cMa complexes in THF.

Several quenching studies were also performed in toluene, but values of k_q for a given photosensitizer-quencher pair were consistently lower when compared to values found in THF (See Figure S13 and Table S3 in the SI). This effect is likely due to the non-polar nature of toluene which increases the work term (W_s in equation 4) and consequently the energy barrier (ΔG_r in equation 6) for charge separation. Non-polar media also inhibits physical separation of the charged species in the cage complex (PS^+,Q^-), which can allow the rate of k_{bet} to become competitive with k_{et}. This effect is expected to lower the overall efficiency of charge transfer, and thus k_q. Alternatively, several quenching studies were performed in MeCN (Table S4). Quenching rates for a given photosensitizer-quencher pair are faster in highly polar MeCN than in THF since the work term becomes negligible in MeCN, which yields a larger driving force in ΔG and a concomitant increase in k_q. However, the benefit from the faster quenching rate is offset by the hypsochromic shift for the ICT transition in MeCN, which decreases the amount light absorbed within the visible portion of the solar spectrum, and significantly decreased excited state lifetimes

5. Conclusion

Photophysical investigations into the excited state redox properties of two-coordinate coinage metal complexes demonstrate that these compounds are a viable new class of photosensitizers for solar fuels applications. Figures of merit were investigated in a variety of different solvents for three new Cu(I) and Au(I) cMa complexes. All reported complexes efficiently absorb visible photons and are potent photo-reducing agents with long-lived excited states. Electrochemical studies show that substituents at the 3,6-position of carbazole stabilizes the cationic species generated upon oxidation. The Au(I) complex has twice the molar absorptivity and greater electrochemical stability compared to Cu(I) analog, with only a minor decrease in excited state reduction potential (~50 meV). The excited state oxidation potential determined using two different methods is found to be $\geq$ -2.3 V vs. $Fc^{+/0}$, which is at a stronger potential than the common scarce metal photosensitizers such as $Ru(bpy)_3^{2+}$ ($E^{+/*}$ = -1.12 V vs. $Fc^{+/0}$) and $Ir(ppy)_3$ ($E^{+/*}$ = -2.14 V vs. $Fc^{+/0}$). Two-coordinate cMa complexes also have excited state reduction potentials greater than Cu(I) bis phenanthroline systems, ($E^{+/*}$ = -1.8 V vs. $Fc^{+/0}$).[4]

Importantly, the choice of carbene largely determines the value for $E^+/*$, whereas the amide determines the value for $E^{*/-}$. Thus, two-coordinate cMa complexes can be modified to make even more potent photo-reducing agents using carbenes with more negative reduction potentials than the carbene used here; however, such a change will shift the lowest energy absorption bands into the near-UV spectrum. These ICT transitions can be shifted back into the visible spectrum by pairing such carbenes with amides that are oxidized at lower potentials. Alternatively, carbenes with less negative reduction potentials than MAC will redshift the absorption deeper into the visible spectrum but are expected to lower the potential for $E^+/*$, making them weaker photoreducing agents. Similarly, amides such as cyano-substituted carbazole ligands can be used to increase the $E^{*/-}$ for photo-oxidative chemistry. Therefore, these cMa complexes can be designed to activate any given electrocatalysts with significant control over the energy of the visible absorption transition, which makes them a promising new class of photosensitizers to produce solar fuels.

Author Information

Corresponding Author

Mark E. Thompson − Department of Chemistry, University of Southern California, Los Angeles, California 90089, United States; orcid.org/0000-0002-7764-4096; Email: met@ usc.edu

Authors

Collin N. Muniz − Department of Chemistry, University of Southern California, Los Angeles, California 90089, United States; orcid.org/0000-0003-4383-6353

Claire A. Archer − Department of Chemistry, University of Southern California, Los Angeles, California 90089, United States

Jack S. Applebaum − Department of Chemistry, University of Southern California, Los Angeles, California 90089, United States

Jonas Schaab − Department of Chemistry, University of Southern California, Los Angeles, California 90089, United States

Peter I. Djurovich − Department of Chemistry, University of Southern California, Los Angeles, California 90089, United States; orcid.org/0000-0001-6716-389

Author Contributions

[†]Authors C.N.M and C.A.A contributed equally to this work.

Acknowledgements

The authors would like to acknowledge the Department of Energy, Office of Basic Energy Science (Award: DE-SC0016450) for support. We also thank the National Science Foundation (Award: CHE-2018740) for funds used to acquire the X-ray diffractometer that was used to determine the crystal structures reported here. In addition, we thank National Science Foundation (DBI-0821671, CHE-0840366) and National Institute of Health (S10 RR25432) for funds to acquire the NMR spectrometers used in our work.

Statement of competing interests: One of the authors, Mark Thompson, has a financial interest in the Universal Display Corporation, one or the funding sources of this work.

References

(1) Kärkäs, M. D.; Verho, O.; Johnston, E. V.; Åkermark, B. Artificial Photosynthesis: Molecular Systems for Catalytic Water Oxidation. *Chemical Reviews* **2014**, *114* (24), 11863-12001. DOI: 10.1021/cr400572f.
(2) Cheung, K. P. S.; Sarkar, S.; Gevorgyan, V. Visible Light-Induced Transition Metal Catalysis. *Chemical Reviews* **2022**, *122* (2), 1543-1625. DOI: 10.1021/acs.chemrev.1c00403.
(3) Bevernaegie, R.; Wehlin, S. A. M.; Piechota, E. J.; Abraham, M.; Philouze, C.; Meyer, G. J.; Elias, B.; Troian-Gautier, L. Improved Visible Light Absorption of Potent Iridium(III) Photooxidants for Excited-State Electron Transfer Chemistry. *Journal of the American Chemical Society* **2020**, *142* (6), 2732-2737. DOI: 10.1021/jacs.9b12108.
(4) Prier, C. K.; Rankic, D. A.; MacMillan, D. W. C. Visible Light Photoredox Catalysis with Transition Metal Complexes: Applications in Organic Synthesis. *Chemical Reviews* **2013**, *113* (7), 5322-5363. DOI: 10.1021/cr300503r.
(5) Larsen, C. B.; Wenger, O. S. Photoredox Catalysis with Metal Complexes Made from Earth-Abundant Elements. *Chemistry – A European Journal* **2018**, *24* (9), 2039-2058, https://doi.org/10.1002/chem.201703602. DOI: https://doi.org/10.1002/chem.201703602 (acccessed 2023/01/08).
(6) Hockin, B. M.; Li, C.; Robertson, N.; Zysman-Colman, E. Photoredox catalysts based on earth-abundant metal complexes. *Catalysis Science & Technology* **2019**, *9* (4), 889-915, 10.1039/C8CY02336K. DOI: 10.1039/C8CY02336K.
(7) Chan, A. Y.; Perry, I. B.; Bissonnette, N. B.; Buksh, B. F.; Edwards, G. A.; Frye, L. I.; Garry, O. L.; Lavagnino, M. N.; Li, B. X.; Liang, Y.; et al. Metallaphotoredox: The Merger of Photoredox and Transition Metal Catalysis. *Chem. Rev.* **2022**, *122* (2), 1485-1542. DOI: 10.1021/acs.chemrev.1c00383.
(8) Hossain, A.; Bhattacharyya, A.; Reiser, O. Copper's rapid ascent in visible-light photoredox catalysis. *Science* **2019**, *364* (6439). DOI: 10.1126/science.aav9713 From NLM PubMed-not-MEDLINE.
(9) Lazorski, M. S.; Castellano, F. N. Advances in the light conversion properties of Cu(I)-based photosensitizers. *Polyhedron* **2014**, *82*, 57-70. DOI: https://doi.org/10.1016/j.poly.2014.04.060.
(10) McMillin, D. R.; Buckner, M. T.; Ahn, B. T. A light-induced redox reaction of bis(2,9-dimethyl-1,10-phenanthroline)copper(I). *Inorganic Chemistry* **1977**, *16* (4), 943-945. DOI: 10.1021/ic50170a046.
(11) Zhang, Y.; Schulz, M.; Wächtler, M.; Karnahl, M.; Dietzek, B. Heteroleptic diimine–diphosphine Cu(I) complexes as an alternative towards noble-metal based photosensitizers: Design strategies, photophysical properties and perspective applications. *Coordination Chemistry Reviews* **2018**, *356*, 127-146. DOI: https://doi.org/10.1016/j.ccr.2017.10.016.
(12) Alkan-Zambada, M.; Hu, X. Cu Photoredox Catalysts Supported by a 4,6-Disubstituted 2,2′-Bipyridine Ligand: Application in Chlorotrifluoromethylation of Alkenes. *Organometallics* **2018**, *37* (21), 3928-3935. DOI: 10.1021/acs.organomet.8b00585.
(13) Cuttell, D. G.; Kuang, S.-M.; Fanwick, P. E.; McMillin, D. R.; Walton, R. A. Simple Cu(I) Complexes with Unprecedented Excited-State Lifetimes. *Journal of the American Chemical Society* **2002**, *124* (1), 6-7. DOI: 10.1021/ja012247h.

(14) Yu, Z.-J.; Chen, H.; Lennox, A. J. J.; Yan, L.-J.; Liu, X.-F.; Xu, D.-D.; Chen, F.; Xu, L.-X.; Li, Y.; Wu, Q.-A.; et al. Heteroleptic copper(I) photosensitizers with carbazole-substituted phenanthroline ligands: Synthesis, photophysical properties and application to photocatalytic H2 generation. *Dyes and Pigments* **2019**, *162*, 771-775. DOI: https://doi.org/10.1016/j.dyepig.2018.10.067.
(15) Hernandez-Perez, A. C.; Collins, S. K. Heteroleptic Cu-Based Sensitizers in Photoredox Catalysis. *Accounts of Chemical Research* **2016**, *49* (8), 1557-1565. DOI: 10.1021/acs.accounts.6b00250.
(16) Sakaki, S.; Kuroki, T.; Hamada, T. Synthesis of a new copper(i) complex, [Cu(tmdcbpy)2]+ (tmdcbpy = 4,4′,6,6′-tetramethyl-2,2′-bipyridine-5,5′-dicarboxylic acid), and its application to solar cells. *Journal of the Chemical Society, Dalton Transactions* **2002**, (6), 840-842, 10.1039/B109518H. DOI: 10.1039/B109518H.
(17) Muniz, C. N.; Schaab, J.; Razgoniaev, A.; Djurovich, P. I.; Thompson, M. E. π-Extended Ligands in Two-Coordinate Coinage Metal Complexes. *Journal of the American Chemical Society* **2022**, *144* (39), 17916-17928. DOI: 10.1021/jacs.2c06948.
(18) Hamze, R.; Peltier, J. L.; Sylvinson, D.; Jung, M.; Cardenas, J.; Haiges, R.; Soleilhavoup, M.; Jazzar, R.; Djurovich, P. I.; Bertrand, G.; et al. Eliminating nonradiative decay in Cu(I) emitters: >99% quantum efficiency and microsecond lifetime. *Science* **2019**, *363* (6427), 601. DOI: 10.1126/science.aav2865.
(19) Hamze, R.; Idris, M.; Muthiah Ravinson, D. S.; Jung, M. C.; Haiges, R.; Djurovich, P. I.; Thompson, M. E. Highly Efficient Deep Blue Luminescence of 2-Coordinate Coinage Metal Complexes Bearing Bulky NHC Benzimidazolyl Carbene. *Frontiers in Chemistry* **2020**, *8*, 401, 10.3389/fchem.2020.00401.
(20) Shi, S.; Jung, M. C.; Coburn, C.; Tadle, A.; Sylvinson M. R, D.; Djurovich, P. I.; Forrest, S. R.; Thompson, M. E. Highly Efficient Photo- and Electroluminescence from Two-Coordinate Cu(I) Complexes Featuring Nonconventional N-Heterocyclic Carbenes. *Journal of the American Chemical Society* **2019**, *141* (8), 3576-3588. DOI: 10.1021/jacs.8b12397.
(21) Hamze, R.; Shi, S.; Kapper, S. C.; Muthiah Ravinson, D. S.; Estergreen, L.; Jung, M.-C.; Tadle, A. C.; Haiges, R.; Djurovich, P. I.; Peltier, J. L.; et al. "Quick-Silver" from a Systematic Study of Highly Luminescent, Two-Coordinate, d10 Coinage Metal Complexes. *Journal of the American Chemical Society* **2019**, *141* (21), 8616-8626. DOI: 10.1021/jacs.9b03657.
(22) Yang, J.-G.; Song, X.-F.; Cheng, G.; Wu, S.; Feng, X.; Cui, G.; To, W.-P.; Chang, X.; Chen, Y.; Che, C.-M.; et al. Conformational Engineering of Two-Coordinate Gold(I) Complexes: Regulation of Excited-State Dynamics for Efficient Delayed Fluorescence. *ACS Applied Materials & Interfaces* **2022**, *14* (11), 13539-13549. DOI: 10.1021/acsami.2c01776.
(23) Tang, R.; Xu, S.; Lam, T.-L.; Cheng, G.; Du, L.; Wan, Q.; Yang, J.; Hung, F.-F.; Low, K.-H.; Phillips, D. L.; et al. Highly Robust CuI-TADF Emitters for Vacuum-Deposited OLEDs with Luminance up to 222 200 cd m−2 and Device Lifetimes (LT90) up to 1300 hours at an Initial Luminance of 1000 cd m−2. *Angewandte Chemie International Edition* **2022**, *61* (33), e202203982, https://doi.org/10.1002/anie.202203982. DOI: https://doi.org/10.1002/anie.202203982 (acccessed 2023/01/25).
(24) Bertrand, B.; Romanov, A. S.; Brooks, M.; Davis, J.; Schmidt, C.; Ott, I.; O'Connell, M.; Bochmann, M. Synthesis, structure and cytotoxicity of cyclic (alkyl)(amino) carbene and acyclic carbene complexes of group 11 metals. *Dalton Transactions* **2017**, *46* (45), 15875-15887, 10.1039/C7DT03189K. DOI: 10.1039/C7DT03189K.

(25) Chotard, F.; Sivchik, V.; Linnolahti, M.; Bochmann, M.; Romanov, A. S. Mono- versus Bicyclic Carbene Metal Amide Photoemitters: Which Design Leads to the Best Performance? *Chemistry of Materials* **2020**, *32* (14), 6114-6122. DOI: 10.1021/acs.chemmater.0c01769.
(26) Conaghan, P. J.; Matthews, C. S. B.; Chotard, F.; Jones, S. T. E.; Greenham, N. C.; Bochmann, M.; Credgington, D.; Romanov, A. S. Highly efficient blue organic light-emitting diodes based on carbene-metal-amides. *Nature Communications* **2020**, *11* (1), 1758. DOI: 10.1038/s41467-020-15369-8.
(27) Gernert, M.; Balles-Wolf, L.; Kerner, F.; Müller, U.; Schmiedel, A.; Holzapfel, M.; Marian, C. M.; Pflaum, J.; Lambert, C.; Steffen, A. Cyclic (Amino)(aryl)carbenes Enter the Field of Chromophore Ligands: Expanded π System Leads to Unusually Deep Red Emitting CuI Compounds. *Journal of the American Chemical Society* **2020**, *142* (19), 8897-8909. DOI: 10.1021/jacs.0c02234.
(28) McCusker, C. E.; Castellano, F. N. Design of a Long-Lifetime, Earth-Abundant, Aqueous Compatible Cu(I) Photosensitizer Using Cooperative Steric Effects. *Inorganic Chemistry* **2013**, *52* (14), 8114-8120. DOI: 10.1021/ic401213p.
(29) Romanov, A. S.; Jones, S. T. E.; Gu, Q.; Conaghan, P. J.; Drummond, B. H.; Feng, J.; Chotard, F.; Buizza, L.; Foley, M.; Linnolahti, M.; et al. Carbene metal amide photoemitters: tailoring conformationally flexible amides for full color range emissions including white-emitting OLED. *Chemical Science* **2020**, *11* (2), 435-446, 10.1039/C9SC04589A. DOI: 10.1039/C9SC04589A.
(30) Karon, K.; Lapkowski, M. Carbazole electrochemistry: a short review. *Journal of Solid State Electrochemistry* **2015**, *19* (9), 2601-2610. DOI: 10.1007/s10008-015-2973-x.
(31) Epifanovsky, E.; Gilbert, A. T. B.; Feng, X.; Lee, J.; Mao, Y.; Mardirossian, N.; Pokhilko, P.; White, A. F.; Coons, M. P.; Dempwolff, A. L.; et al. Software for the frontiers of quantum chemistry: An overview of developments in the Q-Chem 5 package. *The Journal of Chemical Physics* **2021**, *155* (8), 084801. DOI: 10.1063/5.0055522 (acccessed 2023/01/08).
(32) Lu, T.; Chen, F. Multiwfn: A multifunctional wavefunction analyzer. *Journal of Computational Chemistry* **2012**, *33* (5), 580-592, https://doi.org/10.1002/jcc.22885. DOI: https://doi.org/10.1002/jcc.22885 (acccessed 2023/01/08).
(33) Föller, J.; Marian, C. M. Rotationally Assisted Spin-State Inversion in Carbene–Metal–Amides Is an Artifact. *The Journal of Physical Chemistry Letters* **2017**, *8* (22), 5643-5647. DOI: 10.1021/acs.jpclett.7b02701.
(34) Neogrdy, P.; Kell, V.; Urban, M.; Sadlej, A. J. Ionization potentials and electron affinities of Cu, Ag, and Au: Electron correlation and relativistic effects. *International Journal of Quantum Chemistry* **1997**, *63* (2), 557-565. DOI: 10.1002/(sici)1097-461x(1997)63:2<557::Aid-qua25>3.0.Co;2-3.
(35) Li, T.-y.; Schaab, J.; Djurovich, P. I.; Thompson, M. E. Toward rational design of TADF two-coordinate coinage metal complexes: understanding the relationship between natural transition orbital overlap and photophysical properties. *Journal of Materials Chemistry C* **2022**, *10* (12), 4674-4683, 10.1039/D2TC00163B. DOI: 10.1039/D2TC00163B.
(36) Fischer, S.; Rösel, A.; Kammer, A.; Barsch, E.; Schoch, R.; Junge, H.; Bauer, M.; Beller, M.; Ludwig, R. Diferrate [Fe2(CO)6(μ-CO){μ-P(aryl)2}]− as Self-Assembling Iron/Phosphor-Based Catalyst for the Hydrogen Evolution Reaction in Photocatalytic Proton Reduction—Spectroscopic Insights. *Chemistry – A European Journal* **2018**, *24* (60), 16052-16065, https://doi.org/10.1002/chem.201802694. DOI: https://doi.org/10.1002/chem.201802694 (acccessed 2023/01/08).

(37) Natali, M. Elucidating the Key Role of pH on Light-Driven Hydrogen Evolution by a Molecular Cobalt Catalyst. *ACS Catalysis* **2017**, *7* (2), 1330-1339. DOI: 10.1021/acscatal.6b03087.
(38) Khnayzer, R. S.; McCusker, C. E.; Olaiya, B. S.; Castellano, F. N. Robust Cuprous Phenanthroline Sensitizer for Solar Hydrogen Photocatalysis. *Journal of the American Chemical Society* **2013**, *135* (38), 14068-14070. DOI: 10.1021/ja407816f.
(39) Pellegrin, Y.; Sandroni, M.; Blart, E.; Planchat, A.; Evain, M.; Bera, N. C.; Kayanuma, M.; Sliwa, M.; Rebarz, M.; Poizat, O.; et al. New Heteroleptic Bis-Phenanthroline Copper(I) Complexes with Dipyridophenazine or Imidazole Fused Phenanthroline Ligands: Spectral, Electrochemical, and Quantum Chemical Studies. *Inorganic Chemistry* **2011**, *50* (22), 11309-11322. DOI: 10.1021/ic2006343.
(40) Ruthkosky, M.; Castellano, F. N.; Meyer, G. J. Photodriven Electron and Energy Transfer from Copper Phenanthroline Excited States. *Inorganic Chemistry* **1996**, *35* (22), 6406-6412. DOI: 10.1021/ic960503z.
(41) Das, S.; Rodrigues, R. R.; Lamb, R. W.; Qu, F.; Reinheimer, E.; Boudreaux, C. M.; Webster, C. E.; Delcamp, J. H.; Papish, E. T. Highly Active Ruthenium CNC Pincer Photocatalysts for Visible-Light-Driven Carbon Dioxide Reduction. *Inorganic Chemistry* **2019**, *58* (12), 8012-8020. DOI: 10.1021/acs.inorgchem.9b00791.
(42) Huckaba, A. J.; Shirley, H.; Lamb, R. W.; Guertin, S.; Autry, S.; Cheema, H.; Talukdar, K.; Jones, T.; Jurss, J. W.; Dass, A.; et al. A Mononuclear Tungsten Photocatalyst for H2 Production. *ACS Catalysis* **2018**, *8* (6), 4838-4847. DOI: 10.1021/acscatal.7b04242.
(43) Tinker, L. L.; Bernhard, S. Photon-Driven Catalytic Proton Reduction with a Robust Homoleptic Iridium(III) 6-Phenyl-2,2′-bipyridine Complex ([Ir(C/\N/\N)2]+). *Inorganic Chemistry* **2009**, *48* (22), 10507-10511. DOI: 10.1021/ic900777g.
(44) Ma, B.; Djurovich, P.; Thompson, M. Excimer and electron transfer quenching studies of a cyclometalated platinum complex. *Coordination Chemistry Reviews* **2005**, *249*, 1501-1510. DOI: 10.1016/j.ccr.2005.02.004.
(45) Rosspeintner, A.; Kattnig, D. R.; Angulo, G.; Landgraf, S.; Grampp, G. The Rehm–Weller Experiment in View of Distant Electron Transfer. *Chemistry – A European Journal* **2008**, *14* (20), 6213-6221, https://doi.org/10.1002/chem.200701841. DOI: https://doi.org/10.1002/chem.200701841 (acccessed 2023/01/26).
(46) Fukuzumi, S.; Fujita, M.; Otera, J.; Fujita, Y. Electron-transfer oxidation of ketene silyl acetals and other organosilanes. Mechanistic insight into Lewis acid mediated electron transfer. *Journal of the American Chemical Society* **1992**, *114* (26), 10271-10278.
(47) Jones, W. E., Jr.; Fox, M. A. Determination of Excited-State Redox Potentials by Phase-Modulated Voltammetry. *The Journal of Physical Chemistry* **1994**, *98* (19), 5095-5099. DOI: 10.1021/j100070a025.
(48) Scandola, F.; Balzani, V. Free-energy relationships for electron-transfer processes. *Journal of the American Chemical Society* **1979**, *101* (20), 6140-6142. DOI: 10.1021/ja00514a057.
(49) Rehm, D.; Weller, A. Kinetics of Fluorescence Quenching by Electron and H-Atom Transfer. *Israel Journal of Chemistry* **1970**, *8* (2), 259-271, https://doi.org/10.1002/ijch.197000029. DOI: https://doi.org/10.1002/ijch.197000029 (acccessed 2023/01/09).
(50) Weinkauf, J. R.; Cooper, S. W.; Schweiger, A.; Wamser, C. C. Substituent and Solvent Effects on the Hyperporphyrin Spectra of Diprotonated Tetraphenylporphyrins. *The Journal of Physical Chemistry A* **2003**, *107* (18), 3486-3496. DOI: 10.1021/jp022046f.

Supporting Information

Table of Contents

Synthesis and Characterization 3

Synthesis of 1,3-bis(2,6-diisopropylphenyl)-5,5-dimethyl-4-oxo-3,4,5,6-tetrahydropyrimidin-1-ium-2-ide-Cu(I)-3,6-di-tert-butylcarbazol-9-ide (**CuBCzMAC**): 3

Synthesis of 1,3-bis(2,6-diisopropylphenyl)-5,5-dimethyl-4-oxo-3,4,5,6-tetrahydropyrimidin-1-ium-2-ide-Cu(I)-3,6-di-phenylcarbazol-9-ide (**CuPhCzMAC**): 3

Synthesis of 1,3-bis(2,6-diisopropylphenyl)-5,5-dimethyl-4-oxo-3,4,5,6-tetrahydropyrimidin-1-ium-2-ide-Au(I)-3,6-di-tert-butylcarbazol-9-ide (**AuBCzMAC**): 4

Crystal Structures 4

Table S1: Selected bond lengths and angles for the(carbene)M(amide) complexes 5

Table S2. Crystallographic Parameters for $CuBCzMAC$, $AuBCzMAC$ and $CuPhCzMAC$ 6

Computation 7

Figure S1. HOMO and LUMO densities of all reported photosensitizers. 7

Table S1. The percent contribution of the gold atom of AuBCzMAC to the HOMO and LUMO 7

Electrochemistry 8

Figure S2. Reductive DPV sweep of electron accepting quenchers 8

Figure S3. CV and DPV measurements of all reported compounds in DMF vs. $Fc^{+/0}$. 9

Figure S4. CV and DPV measurements of all reported compounds in MeCN vs. $Fc^{+/0}$. 10

Figure S5. CV and DPV measurements of all reported compounds in THF vs. $Fc^{+/0}$. 11

Figure S6. CV measurements of the first oxidation in DCM vs. $Fc^{+/0}$ 12

Photophysics 13

Figure S8. Molar absorptivity spectra in THF 14

Figure S9. Solvent dependent PL of $AuBCzMAC$ 14

Figure S10. Solvent dependent PL of $CuPhCzMAC$: (a) absorption 15

Figure S11. The non-radiative rate vs. solvent ET(30) 15

Figure S12. Stern-Volmer plots measured in THF 17

Figure S13. Stern-Volmer plots measured in Toluene. 18

Figure S14. Stern-Volmer plots measured in MeCN. 19

Table S3. Stern-Volmer results of kq in Toluene 19

Table S4. Stern-Volmer results of kq in MeCN 19

Table S5. Parameters from Rehm-Weller fit of kq vs. E0/- 20

^{1}H and ^{13}C NMR Spectra 22

Figure S15. ^{1}H and ^{13}C NMR of CuBCzMAC in acetone-d6 22

Figure S17. ^{1}H and ^{13}C NMR of CuPhCzMAC in acetone-d6 23

Figure S17. ^{1}H and ^{13}C NMR of AuBCzMAC in acetone-d6 24

Synthesis and Characterization

Synthesis of 1,3-bis(2,6-diisopropylphenyl)-5,5-dimethyl-4-oxo-3,4,5,6-tetrahydropyrimidin-1-ium-2-ide-Cu(I)-3,6-di-tert-butylcarbazol-9-ide ($\mathbf{Cu}_{\mathbf{BCz}}^{\mathbf{MAC}}$): Following the general procedure, a 150 mL Schlenkflask was charged with 512 mg 3,6-di-tert-butyl-9-H-carbazole (1.83 mols) and 185 mg sodium tert-butoxide (1.92 mols). The solids were dissolved in 80 mL THF, and 1.0 g (1.83 mols) of MAC CuCl was added. The workup yielded a yellow powder. The powder was washed with methanol which dissolved some product but removed all remaining impurities, yielding 890 mg (64% yield) of Cu_{BCz}^{MAC} as a yellow powder which is bright yellow emissive under 365 nm UV radiation. ^{1}H NMR (400 MHz, acetone-d6) δ: 7.81-7.72 (m,4H), 7.58 (d, J = 7.6 Hz, 2H), 7.52 (d, J = 7.9 Hz, 2H), 6.90 (dd, J = 8.6 Hz, 2.1 Hz, 2H), 5.52 (d, J = 8.8 Hz, 2H), 4.25 (s, 2H), 3.55 (hept, J = 7.0 Hz, 2H), 3.29 (hept, J = 7.2 Hz, 2H), 1.66 (s, 6H), 1.42 (d, J = 6.8 Hz, 6H), 1.32 (s, 18H), 1.28-1.22 (m, 18H). ^{13}C NMR (100 MHz, acetone-d6) δ: 211.0, 206.3, 206.3, 172.3, 149.5, 147.4, 146.4, 141.5, 138.0, 137.5, 131.3, 130.9, 126.7, 125.8, 124.9, 121.2, 115.3, 115.0, 62.2, 39.0, 35.0, 32.8, 32.5, 30.6, 30.4, 30.2, 30.0, 29.8, 29.8, 29.6, 29.5, 29.4, 25.5, 24.9, 24.7, 24.6, 24.5. CHN (C: 76.61%; H: 8.40%; N: 5.47%; calculated: C: 76.15%; H: 8.44%; N: 5.33%).

Synthesis of 1,3-bis(2,6-diisopropylphenyl)-5,5-dimethyl-4-oxo-3,4,5,6-tetrahydropyrimidin-1-ium-2-ide-Cu(I)-3,6-di-phenylcarbazol-9-ide ($\mathbf{Cu}_{\mathbf{PhCz}}^{\mathbf{MAC}}$): Following the general procedure, a 250 mL Schlenkflask was charged with 585 mg 3,6-diphenyl-9-H-carbazole (1.83 mols) and 185 mg (1.92 mols) NaO^{t}Bu. The solids were dissolved in 100 mL THF, and 1.0 g (1.83 mols) of MAC CuCl was added to yield a light yellow powder after the general workup. The powder was washed copiously with with diethyl ether to afford 1020 mg (67% yield) of Cu_{PhCz}^{MAC} as a shiny yellow powder which emits intense turquoise under 365 nm UV radiation. (400 MHz, acetone-d6) δ: 8.17 (dd, J = 0.7Hz, 2.0 Hz, 2H), 7.87-7.80 (m, 2H), 7.67-7.62 (m, 6H), 7.58 (d, J = 7.8 Hz, 2H), 7.41-7.36 (m, 4H), 7.23-7.18 (m, 4H), 5.66 (dd, J = 0.6 Hz, J = 8.3Hz), 4.30 (s, 2H), 3.59 (hept, J = 6.9Hz, 2H), 3.33 (hept, J = 7.0 Hz, 2H), 1.68 (s, 6H), 1.4 (d, J=6.6 Hz, 6H), 1.33-1.24 (m, 18H). ^{13}C NMR (100 MHz, acetone-d6) δ: 210.7, 206.3, 206.3, 206.3, 172.3, 151.2, 147.5, 146.4, 144.2, 141.5, 137.5, 131.5, 131.1, 129.8, 129.5, 129.4, 127.9, 127.5, 127.3, 126.8, 126.2, 126.1, 125.9, 125.9, 123.5, 119.7, 118.2, 116.1, 62.1, 39.0, 32.4, 30.5, 30.4, 30.3, 30.2, 30.0,

29.8, 29.6, 29.5, 29.4, 29.3, 25.5, 24.9, 24.7, 24.5. CHN (C: 77.70%; H: 6.94%; N: 5.14%; calculated: C: 78.27%; H: 7.06%; N: 5.07%)

Synthesis of 1,3-bis(2,6-diisopropylphenyl)-5,5-dimethyl-4-oxo-3,4,5,6-tetrahydropyrimidin-1-ium-2-ide-Au(I)-3,6-di-tert-butylcarbazol-9-ide ($\mathbf{Au}_{\mathbf{BCz}}^{\mathbf{MAC}}$): Following the general procedure, a 250 mL Schlenkflask was charged with 411 mg (1.47 mols) 3,6-di-tertbutyl-9-H-carbazole and 142 mg NaO^{t}Bu (1.62 mols). The solids were dissolved in 120 mL THF and 1.0g (1.47 mols) MAC AuCl was added. The general workup afforded 425 mg (31% yield) of Au_{BCz}^{MAC}as a mustard yellow powder that emits bright yellow under 365 nm radiation. ^{1}H NMR (400 MHz, acetone-d6) δ: 7.83 (d, J = 2 Hz, 2H), 7.78-7.69 (m, 2H), 7.56 (d, J = 7.7 Hz, 2H), 7.50 (d, J = 7.8 Hz, 2H), 7.0 (dd, J = 1.7 Hz, J = 9.0 Hz, 2H), 6.00 (d, J = 8.6 Hz, 2H), 4.25 (s, 2H), 3.50 (hept, J = 6.8 Hz, 2H), 3.25 (hept, J = 6.8 Hz, 2H), 1.68 (s, 6H), 1.41 (d, J = 6.7 Hz, 6H), 1.37 (d, J = 6.8 Hz, 6H), 1.34 (d, J = 7.4 Hz, 6H), 1.33 (s, 18H), 1.22 (d, J = 6.8 Hz, 6H). ^{13}C NMR (100 MHz, acetone-d6) δ 206.3, 206.3, 206.2, 205.7, 173.0, 149.1, 147.4, 146.2, 141.7, 138.8, 137.7, 131.1, 130.8, 126.4, 125.4, 124.7, 121.5, 115.5, 114.4, 62.1, 39.1, 35.0, 35.0, 32.8, 32.6, 30.6, 30.6, 30.4, 30.4, 30.2, 30.0, 29.8, 29.8, 29.6, 29.6, 29.4, 25.0, 24.7, 24.7, 24.6, 24.3, 14.8. CHN (C: 64.59%; H: 7.10%; N: 4.63%; calculated: C: 65.13%; H: 7.22%; N: 4.56%).

Crystal Structures

All crystals were grown by recrystallization. Vappordiffusion of hexanes or pentane into a solution of the compound in DCM or Acetone. A Cryo-Loop was used to mount the sample with Paratone oil.

All single crystal structures were determined at 100K with Rigaku Xta LAB Synergy S, equipped with an HyPix-600HE detector and an Oxford Cryostream 800 low Temperature unit, using Cu K_α PhotonJet-S X-ray source. The frames were integrated using the SAINT algorithm to give the hkl files. Data were corrected for absorption effects using the multi-scan method (SADABS) with Rigaku CrysalisPro. The structures were solved by intrinsic phasing and refined with the SHELXTL Software Package. If necessary, the disordered solvent treatment method BYPASS for co-crystalizing solvent molecules, was implemented and marked in the CCDC entry.

All cif files and report data including atom position, bond lengths and bond angle can be downloaded from the CCDC database, using the database number in the right column of the following table. Furthermore the following table is giving the most important bond lengths, angels and the torsion angle around the metal center. The Conformer ratio represents the ratio of two different disordered conformations of the molecule. All crystalized with one molecule in the asymmetric unit.

Table S1: Selected bond lengths and angles for the(carbene)M(amide) complexes.

compound	C-M (A)	M-N (A)	C-M-N (˚)	Torsion (˚) NC-M-NC	C-N-C(O) (˚) C-N-C(H_2) (˚)	Dissorder ratio
Cu_{BCz}^{MAC}	1.875(2)	1.849(2)	178.71	19.62	126.41 124.03	-/-
Au_{BCz}^{MAC}	1.977(4)	1.997(3)	176.23	14.66	124.76 124.03	60/40 (CH_3) 50/50 (C=O)
Cu_{PhCz}^{MAC}	1.882(2)	1.854(2)	175.11	2.22 6.52	125.89 123.46	-/-

Table S2. Crystallographic Parameters for Cu_{BCz}^{MAC}, Au_{BCz}^{MAC} and Cu_{PhCz}^{MAC}

Identification code	$\boldsymbol{Cu_{BCz}^{MAC}}$	$\boldsymbol{Au_{BCz}^{MAC}}$	$\boldsymbol{Cu_{PhCz}^{MAC}}$
Empirical formula	$C_{50}H_{66}CuN_3O$	$C_{50}H_{66}AuN_3O$	$C_{54}H_{58}CuN_3O$
Formula weight	788.59	921.07	828.57
Temperature/K	99.9(3)	100.0(2)	100.0(3)
Crystal system	monoclinic	monoclinic	monoclinic
Space group	$P2_1/n$	$P2_1/n$	$P2_1/c$
a/Å	12.6232(1)	14.7369(2)	17.0684(4)
b/Å	15.5893(1)	13.0901(2)	15.5735(3)
c/Å	23.7886(2)	24.4764(4)	19.4670(4)
α/°	90	90	90
β/°	99.598(1)	107.306(2)	114.062(3)
γ/°	90	90	90
Volume/Å^3	4615.75(6)	4507.93(13)	4725.0(2)
Z	4	4	4
ρ_{calc}g/cm^3	1.135	1.357	1.165
μ/mm^{-1}	0.939	6.412	0.947
F(000)	1696.0	1892.0	1760.0
Crystal size/mm^3	0.162 × 0.216 × 0.326	0.474 × 0.294 × 0.208	0.141 × 0.089 × 0.07
Radiation	Cu Kα (λ = 1.54184)	Cu Kα (λ = 1.54184)	Cu Kα (λ = 1.54184)
2Θ range for data coll./°	6.808 to 154.728	7.566 to 154.978	5.67 to 154.09
Index ranges	$-14 \le h \le 15$, $-19 \le k \le 19$, $-28 \le l \le 30$	$-18 \le h \le 17$, $-15 \le k \le 16$, $-28 \le l \le 30$	$-20 \le h \le 14$, $-18 \le k \le 18$, $-24 \le l \le 23$
Reflections collected	85783	46425	33322
Independent reflections	9360 [R_{int} = 0.0466, R_{sigma} = 0.0214]	8765 [R_{int} = 0.0607, R_{sigma} = 0.0378]	8414 [R_{int} = 0.0451, R_{sigma} = 0.0326]
Data/restraints/parameters	9360/0/512	8765/0/544	8414/0/543
Goodness-of-fit on F^2	1.047	1.027	1.049
Final R indexes [I>=2σ]	R_1= 0.0578, wR_2= 0.1607	R_1= 0.0331, wR_2= 0.0821	R_1= 0.0581, wR_2= 0.1497
Final R indexes [all data]	R_1= 0.0624, wR_2= 0.1648	R_1 = 0.0376, wR_2 = 0.0853	R_1 = 0.0658, wR_2 = 0.1547
Largest diff. peak/hole/e Å^{-3}	2.29/-0.69	0.84/-1.67	0.43/-0.84
#CCDC	**2238026**	**2237840**	**2237833**

Computation

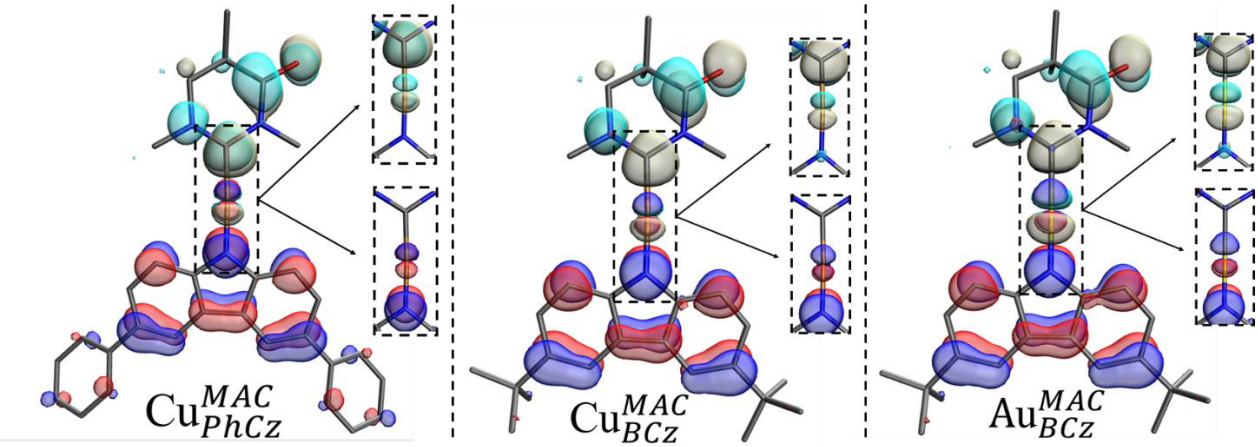

Figure S1. HOMO and LUMO densities of all reported photosensitizers. The HOMO is displayed in red and blue, and the LUMO is displayed in cyan and cream for Cu_{PhCz}^{MAC}, Cu_{BCz}^{MAC}, and Au_{BCz}^{MAC} (iso-value = 0.1). A zoomed in panel is shown for each compound to illustrate that the HOMO and LUMO wavefunctions share density at the metal center. The 3,6-diisopropylphenyl substituents, and hydrogen atoms are deleted for clarity.

Several different methods were used to evaluate the atomic orbital contribution to a given molecular orbital including the Mulliken partition method, the Stout-Politzer partition method, the Ros-Schuit partition, and the Hirshfeld method. Computations were performed using Multiwfn.

Table S1. The percent contribution of the gold atom of Au_{BCz}^{MAC} to the HOMO and LUMO by different computational methods.

MAC Au Cz	HOMO (%)	LUMO (%)
Mulliken	4.3	9.1
Stout-Politzer	3.5	7.9
Ros-Scuit	4.7	6.9
Hirshfeld	3.4	8.4

Electrochemistry

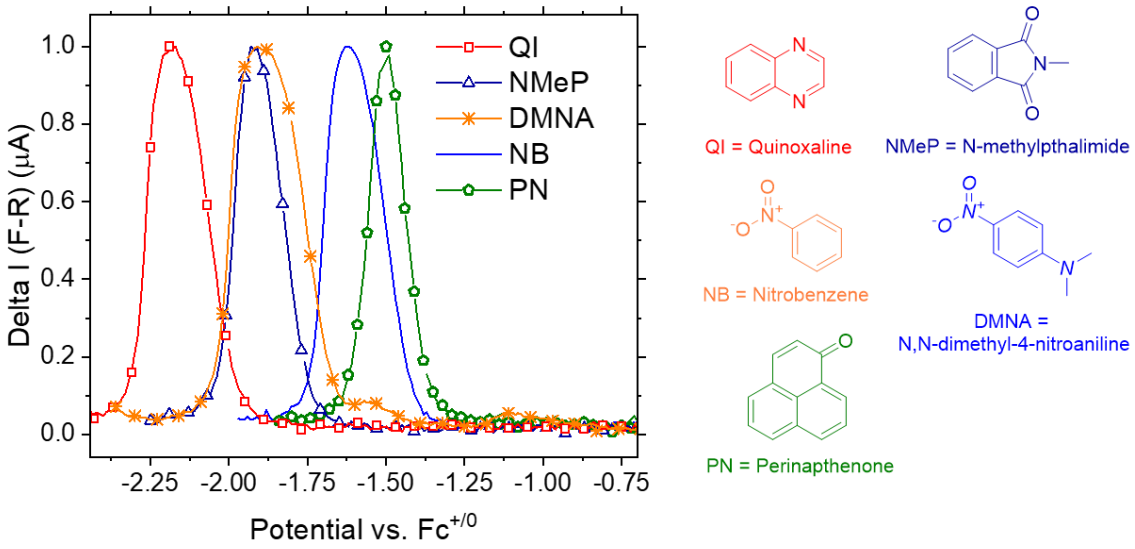

Figure S2. Reductive DPV sweep of electron accepting quenchers that were used to determine $E^{*/+}$ of the cMa complexes.

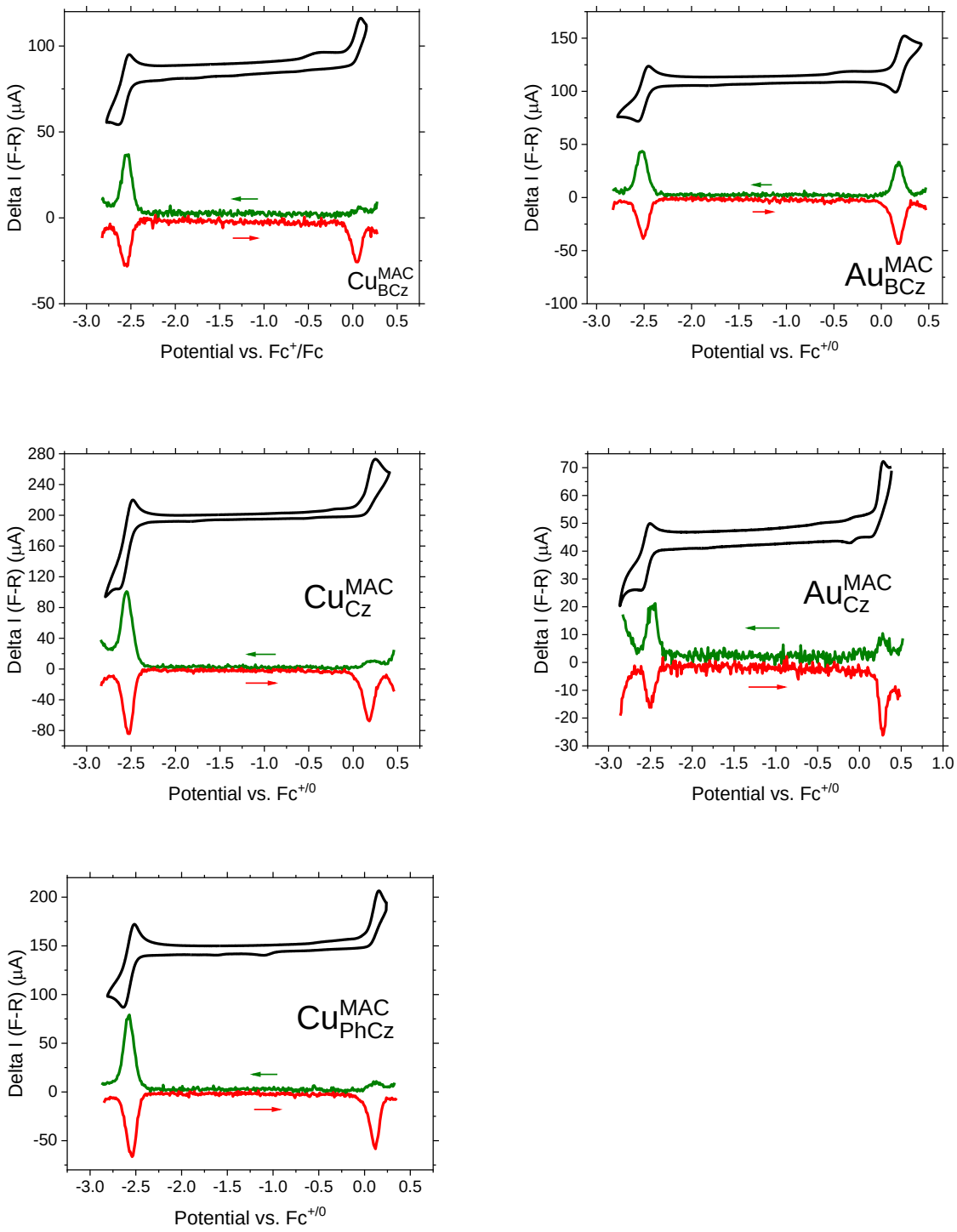

Figure S3. CV and DPV measurements of all reported compounds in DMF vs. $Fc^{+/0}$. The CV scans were vertically shifted to be above the DPV scans during post-processing of the data.

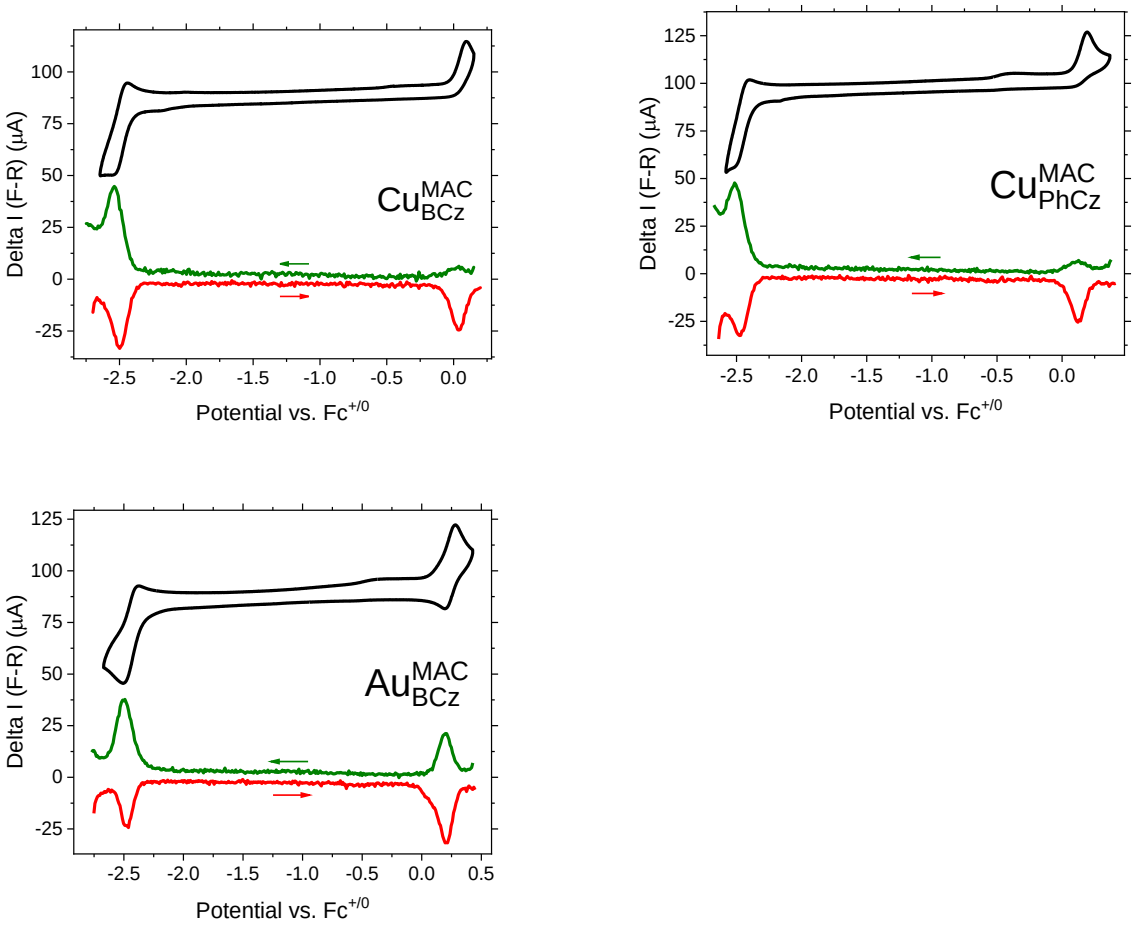

Figure S4. CV and DPV measurements of all reported compounds in MeCN vs. $Fc^{+/0}$. The CV scans were vertically shifted to be above the DPV scans during post-processing of the data.

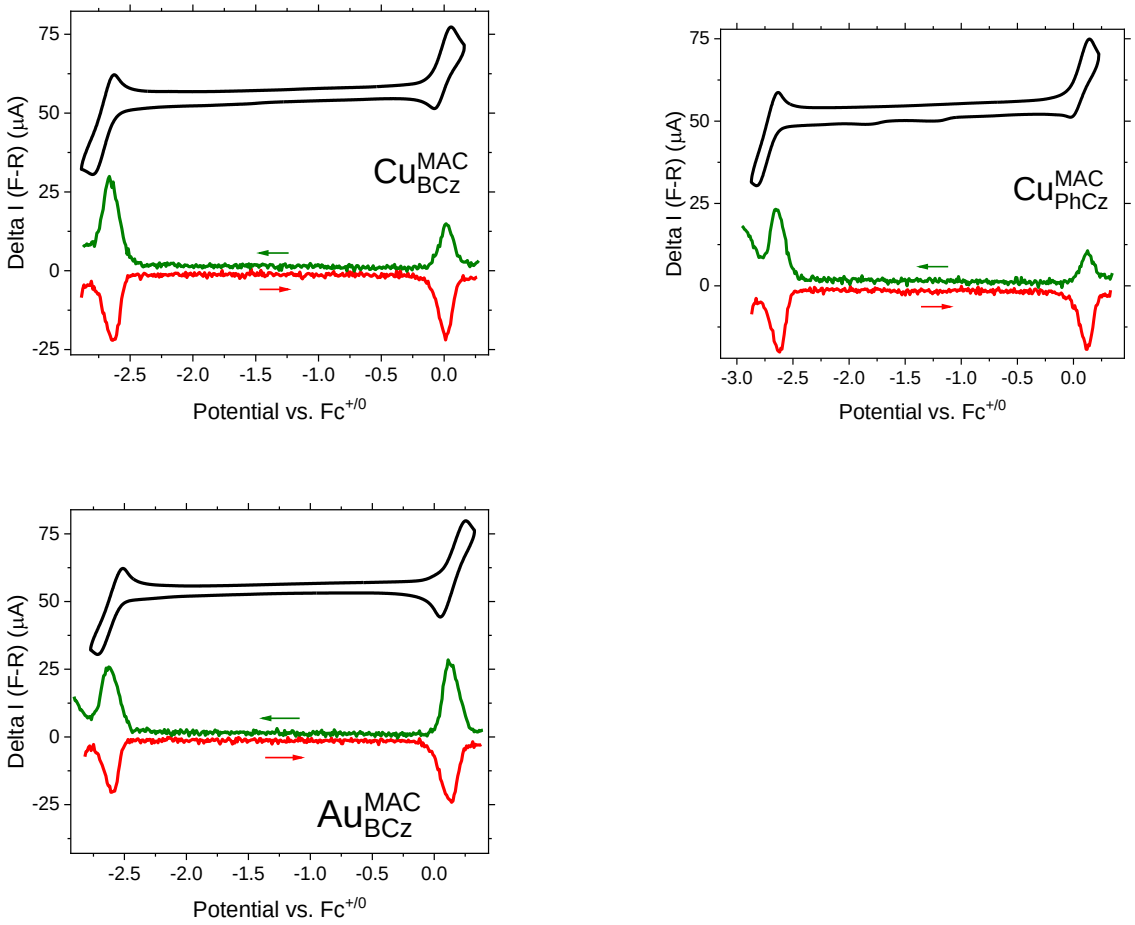

Figure S5. CV and DPV measurements of all reported compounds in THF vs. $Fc^{+/0}$. The CV scans were vertically shifted to be above the DPV scans during post-processing of the data.

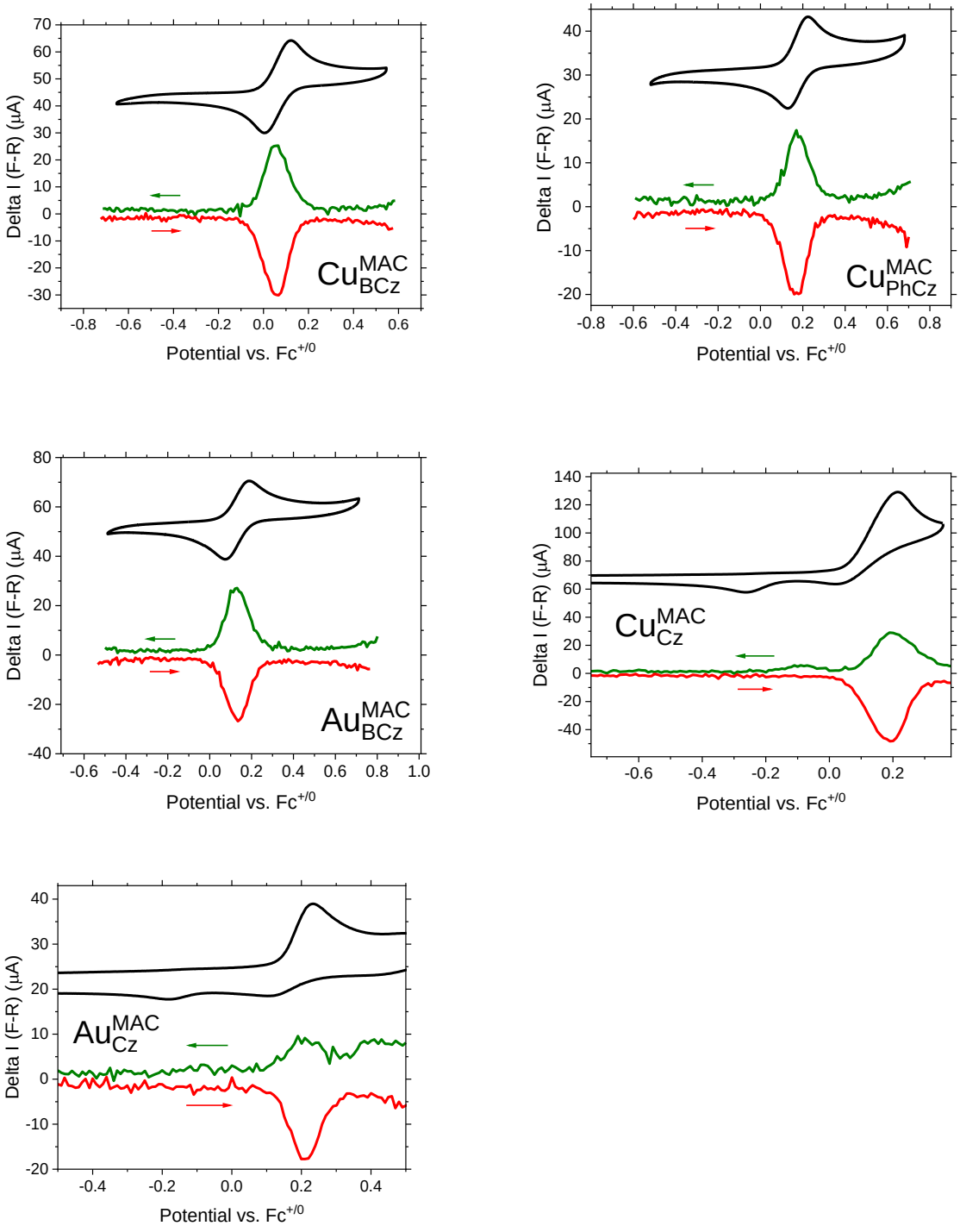

Figure S6. CV measurements of the first oxidation in DCM vs. $Fc^{+/0}$. The reduction event is outside of the solvent window.

Photophysics

Measurements were made in a custom designed glass cuvette equipped with a Teflon valve and side-arm with a small opening. Polyethylene tubing was inserted through the side-arm hole with the schlenk valve open just enough for the tube to pass into the solution and sparge it with N_2. Sparging was performed for ~10 minutes. The tube was raised past the Schlenk valve but not out of the side-arm under high N_2 flow, and the Schlenk valve was sealed to establish a N_2 atmosphere in the samples. Finally, the tube was removed from the side-arm.

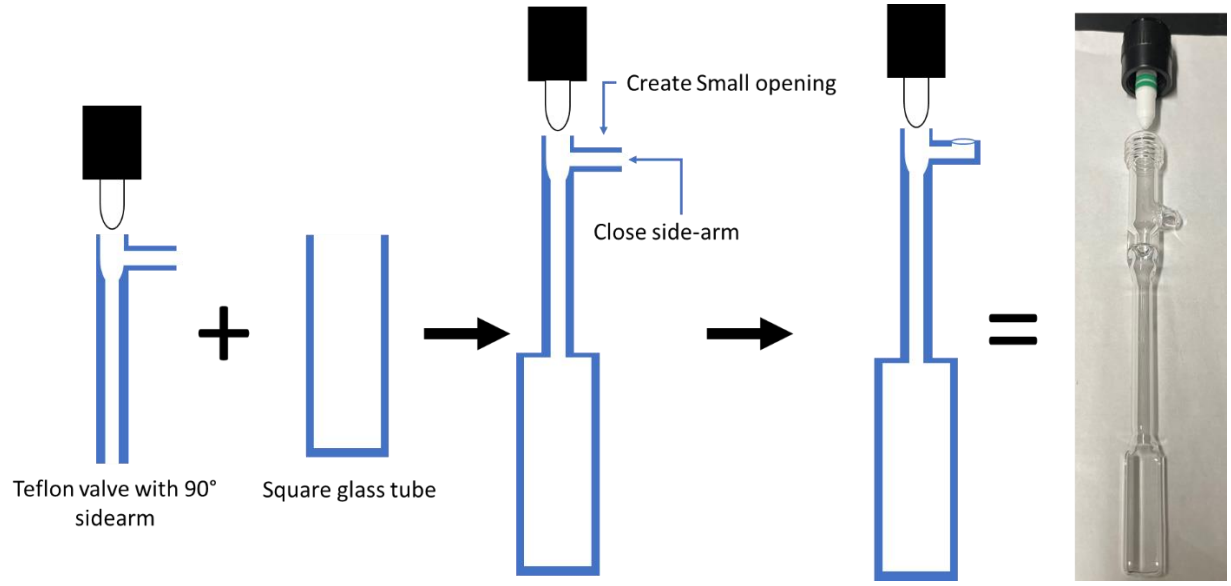

Figure S7. Custom Schlenk cuvettes were made by purchasing a glass joint with a Teflon valve and 90° side-arm. This was fused to a 1cmx1cm square glass tube with the bottom sealed to form the cuvette shape. The side-arm was sealed and a smaller opening was created to make a smaller inlet for the sparging tubing.

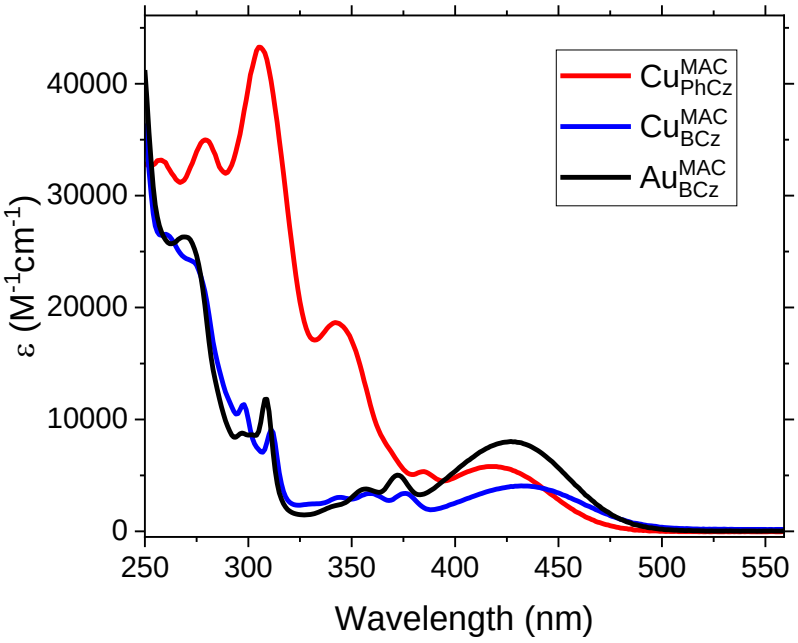

Figure S8. Molar absorptivity spectra in THF for all reported photosensitizers.

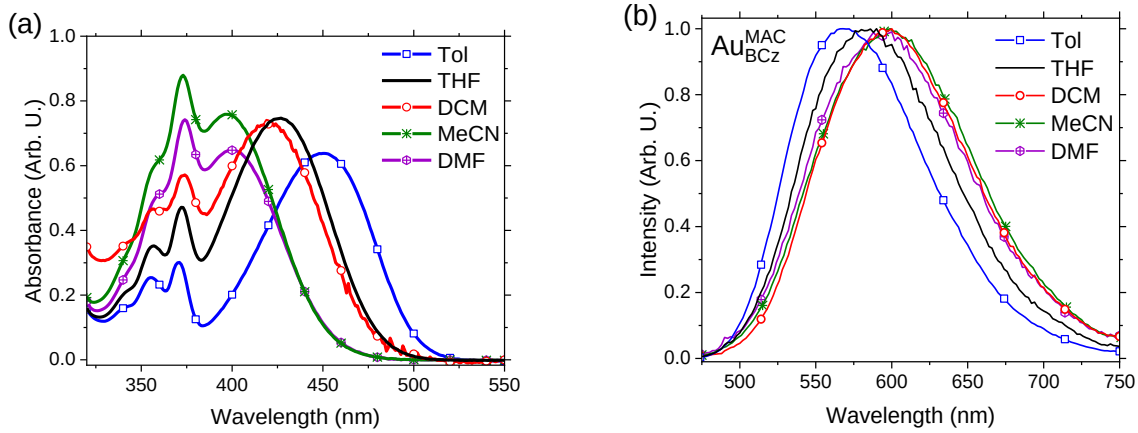

Figure S9. Solvent dependent PL of Au_{BCz}^{MAC}: (a) absorption, (b) emission.

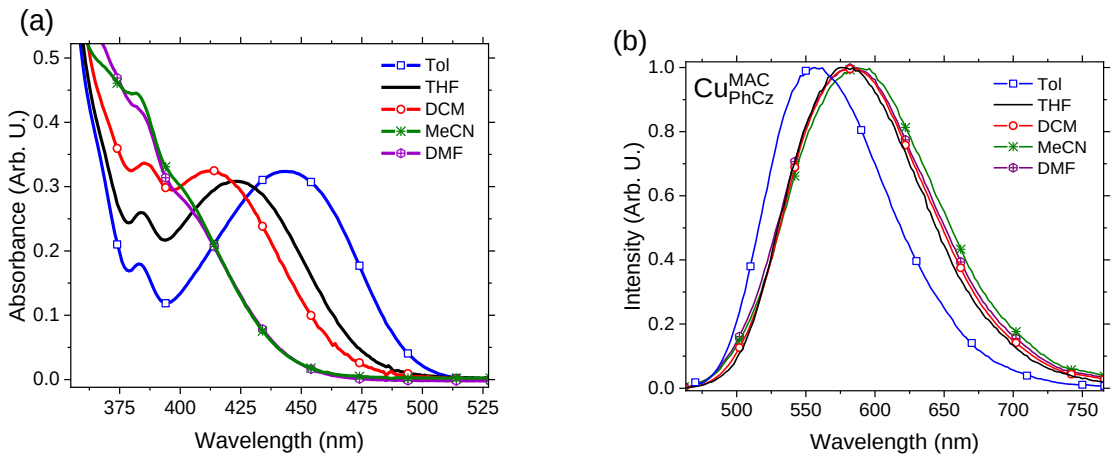

Figure S10. Solvent dependent PL of Cu_{PhCz}^{MAC}: (a) absorption, (b) emission.

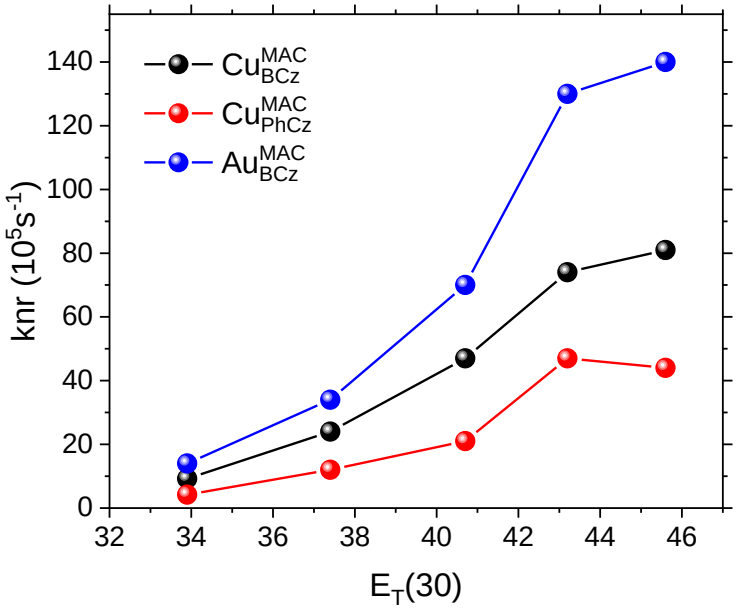

Figure S11. The non-radiative rate vs. solvent ET(30) of all reported photosensitizers.[50]

Au_{BCz}^{MAC}:

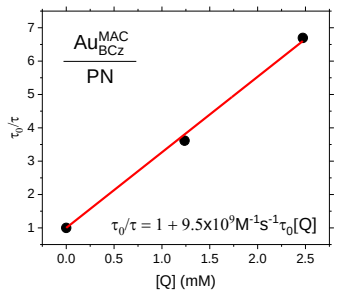

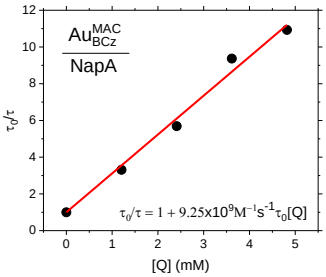

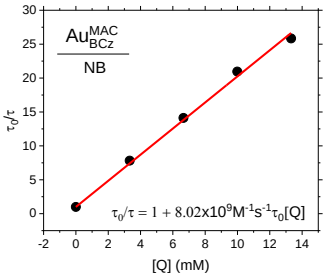

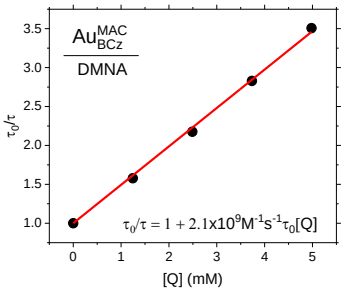

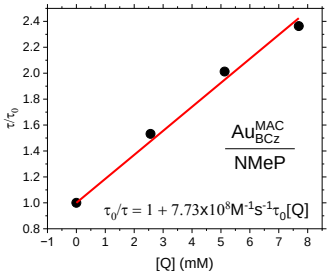

Cu_{BCz}^{MAC}:

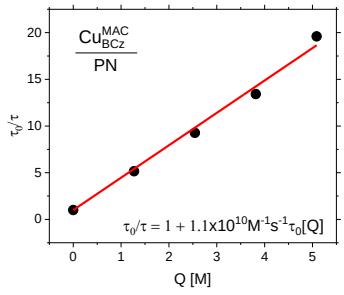

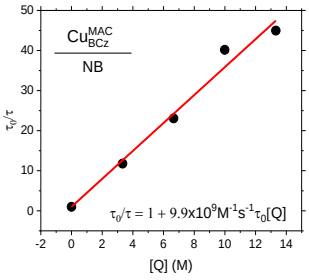

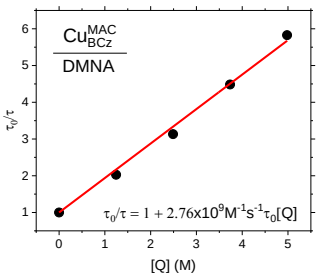

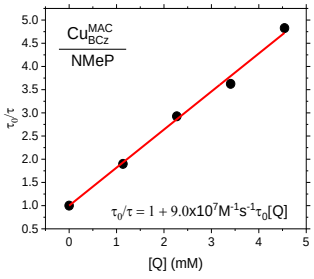

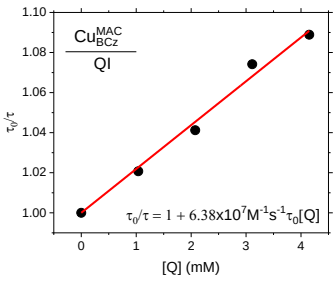

Cu_{PhCz}^{MAC}:

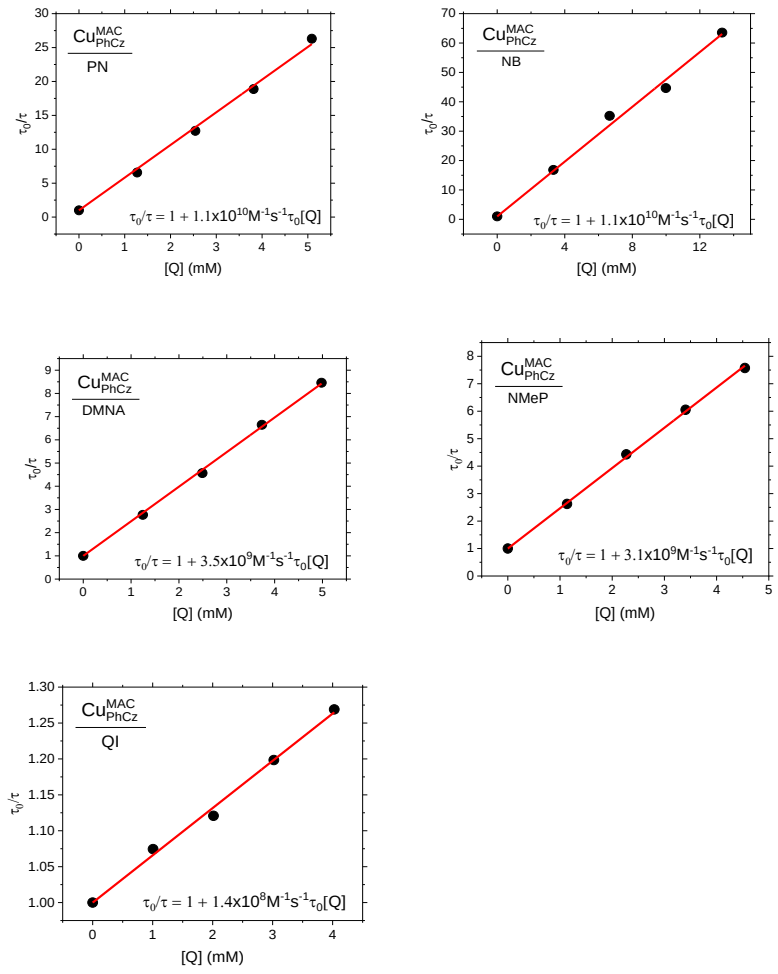

Figure S12. Stern-Volmer plots measured in THF. The corresponding photosensitizer and electron accepting quencher are displayed on the plots.

Cu_{BCz}^{MAC}:

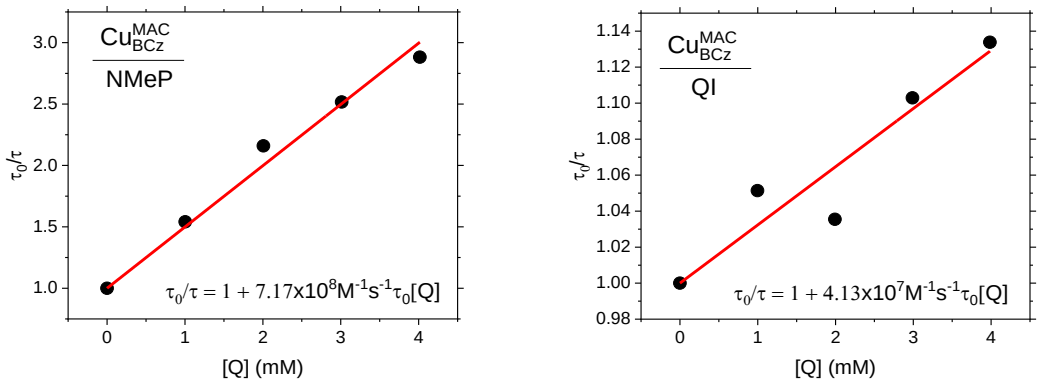

Cu_{PhCz}^{MAC}:

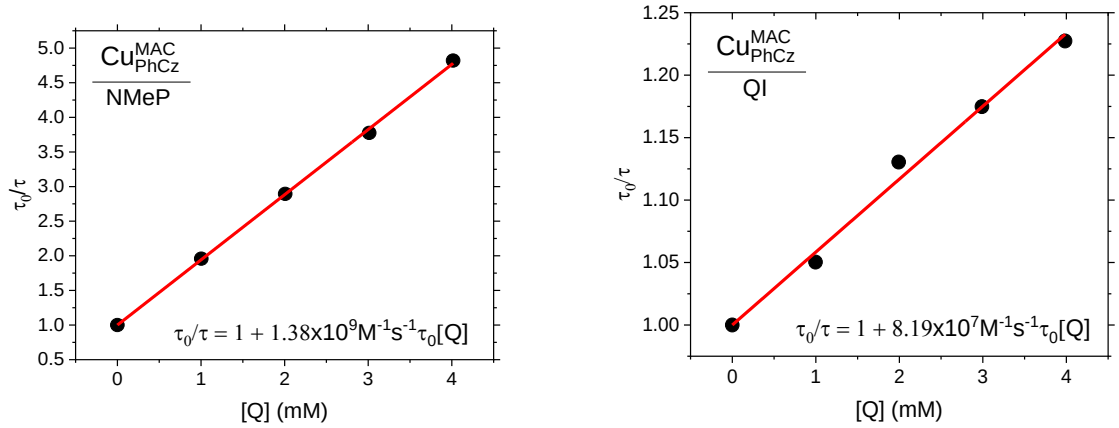

Figure S13. Stern-Volmer plots measured in Toluene. The corresponding photosensitizer and electron accepting quencher are displayed on the plots

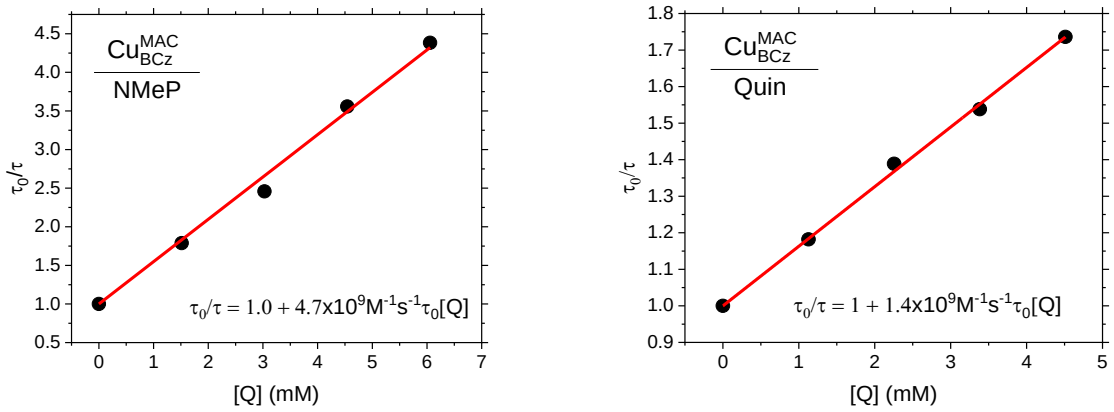

Figure S14. Stern-Volmer plots measured in MeCN. The corresponding photosensitizer and electron accepting quencher are displayed on the plots.

Table S3. Stern-Volmer results of kq in Toluene for all cpds against quinoxaline and n-methyl pthalimide. Au_{BCz}^{MAC} did not yield measurable k_q with quinoxaline or NMeP as an electron accepting quencher.

	V_{red}(V)	$k_q(Cu_{BCz}^{MAC})$ ($M^{-1}s^{-1}10^9$)	$k_q(Cu_{PhCz}^{MAC})$ ($M^{-1}s^{-1}10^9$)
Quin	-2.18	0.04	0.08
NMeP	-1.92	0.71	1.38

Table S4. Stern-Volmer results of kq in MeCN for all cpds against quinoxaline and n-methyl pthalimide.

	V_{red}(V)	$k_q(Cu_{BCz}^{MAC})$ ($M^{-1}s^{-1}10^9$)
Quin	-2.18	1.4
NMeP	-1.92	4.7

A Rehm-Weller analysis was performed using Equations (4) - (6) in the main text which are re-printed here for reference:

$$\Delta G = \left(E_{PS}^{+/*} - E_{Q}^{0/-}\right) + W_s \quad (4)$$

$$k_q = \frac{k_d}{1 + \left(\frac{k_d}{\Delta V_{12} \times k_{re}}\right)\left(\exp\left(\frac{\Delta G^{\ddagger}}{RT}\right) + \exp\left(\frac{\Delta G}{RT}\right)\right)} \quad (5)$$

$$\Delta G^{\ddagger} = \left[\left(\frac{\Delta G}{2}\right)^2 + (\Delta G_r)^2\right]^{\frac{1}{2}} + \frac{\Delta G}{2} \quad (6)$$

Where $E_{PS}^{+/*}$ is the excited state oxidation potential of the photosensitizer, $E_{Q}^{0/-}$ is the reduction potential of the quenching molecule, W_S is the work term associated with the solvent, R is the ideal gas constant, T is temperature.[49] The free energy term $\Delta G^{\ddagger}$ accounts for the reorganization energy of (PS^*,Q) to (PS^+,Q^-) and the solvent reorganization required for electron transfer ΔG_r. The rate constants k_d, k_{-d}, and k_{re} are from the kinetic scheme shown in Figure 7 of the main paper. ΔV_{12} is the equilibrium constant between k_d and k_{-d}.

Fitting k_q vs. $E^{0/-}$ of the quenching molecule provides values of all parameters in equations 4-6 including $E^{+/*}$, W_S, k_d, k_{-d}, k_{re}, and ΔG_r. The reverse process k_{-d} is typically near equivalent to k_d, so ΔV_{12} was set to unity. This yielded the following parameter values with less than 1% error:

Table S5. Parameters from Rehm-Weller fit of kq vs. E0/- of the quenching molecule.

	$E^{+/*}$ (V vs. $Fc^{+/0}$)	**ΔG_r (eV)**	**W_S (eV)**	**k_{re} (s^{-1})**
$\mathbf{Cu_{BCz}^{MAC}}$	-2.28	0.25	0.1	4.0 x 10^3
$\mathbf{Cu_{PhCz}^{MAC}}$	-2.33	0.25	0.1	4.0 x 10^3
$\mathbf{Au_{BCz}^{MAC}}$	-2.23	0.25	0.1	4.0 x 10^3

The trend in excited state oxidation potential is consistent with the Stern-Volmer quenching experiments. For a given quenching molecule in a given solvent, the measured k_q always increases in the order of Au_{BCz}^{MAC} < Cu_{BCz}^{MAC} < Cu_{PhCz}^{MAC}. The Rehm-Weller analysis suggests that this is due to the difference in reductive potency of the excited state $E^{+/*}$ which follows the same trend: Au_{BCz}^{MAC} < Cu_{BCz}^{MAC} < Cu_{PhCz}^{MAC}. The solvent reorganization term ΔG_r is within the typical range compared to

other reported systems.[3, 49] The value is consistent for all photosensitizers which can be explained by the similar structural motif of the photosensitizers; they are all two-coordinate carbene-metal amides. The solvent work term of 0.1 eV is reasonable and consistent between all photosensitizers which is to be expected, because W_S is an intrinsic property of the solvent.[44] Lastly, k_{re} is consistent between all photosensitizers and suggests the charge separated pair (PS^+,Q^-) recombines to the ground state (PS,Q) with a time constant of 250μs.

^{1}H and ^{13}C NMR Spectra

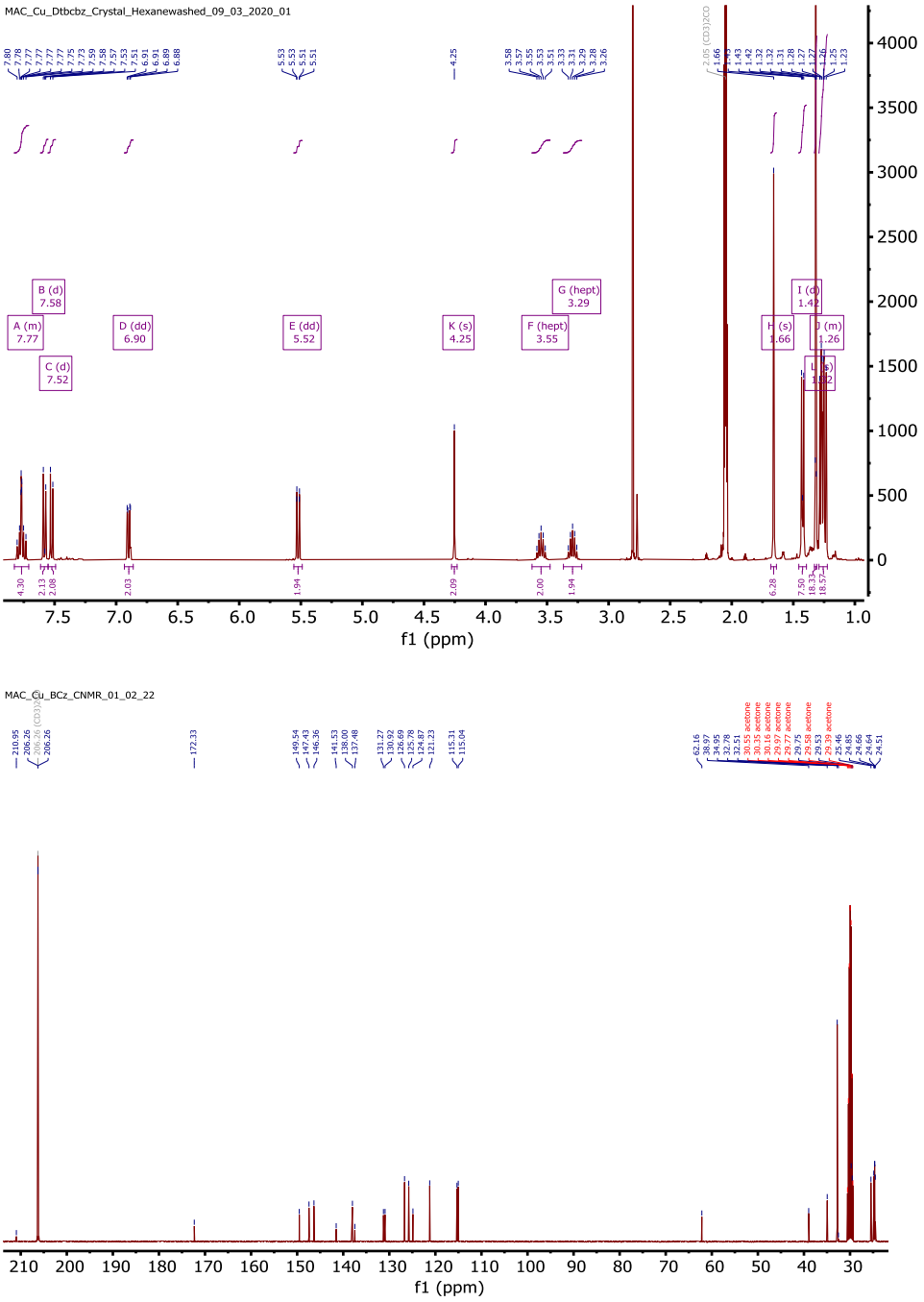

Figure S15. ^{1}H and ^{13}C NMR of Cu_{BCz}^{MAC} in acetone-d6. The peaks at 2.05ppm and 2.8ppm in the ^{1}H NMR correspond to acetone and water respectively.

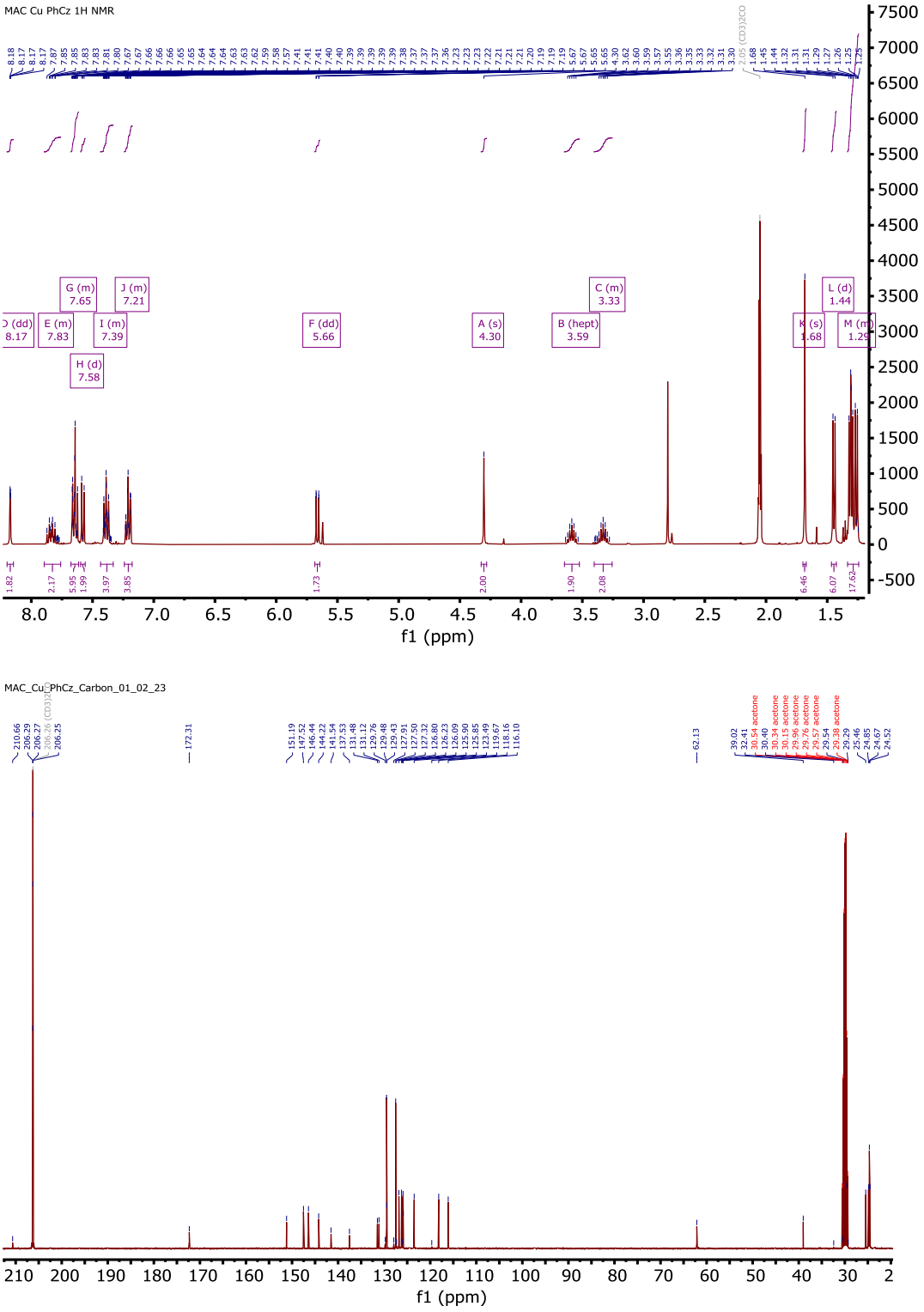

Figure S17. ^{1}H and ^{13}C NMR of Cu^{MAC}_{PhCz} in acetone-d6. The peaks at 5.2ppm, 2.8ppm, and 2.05ppm in the ^{1}H NMR correspond to DCM, water, and acetone-d6 respectively.

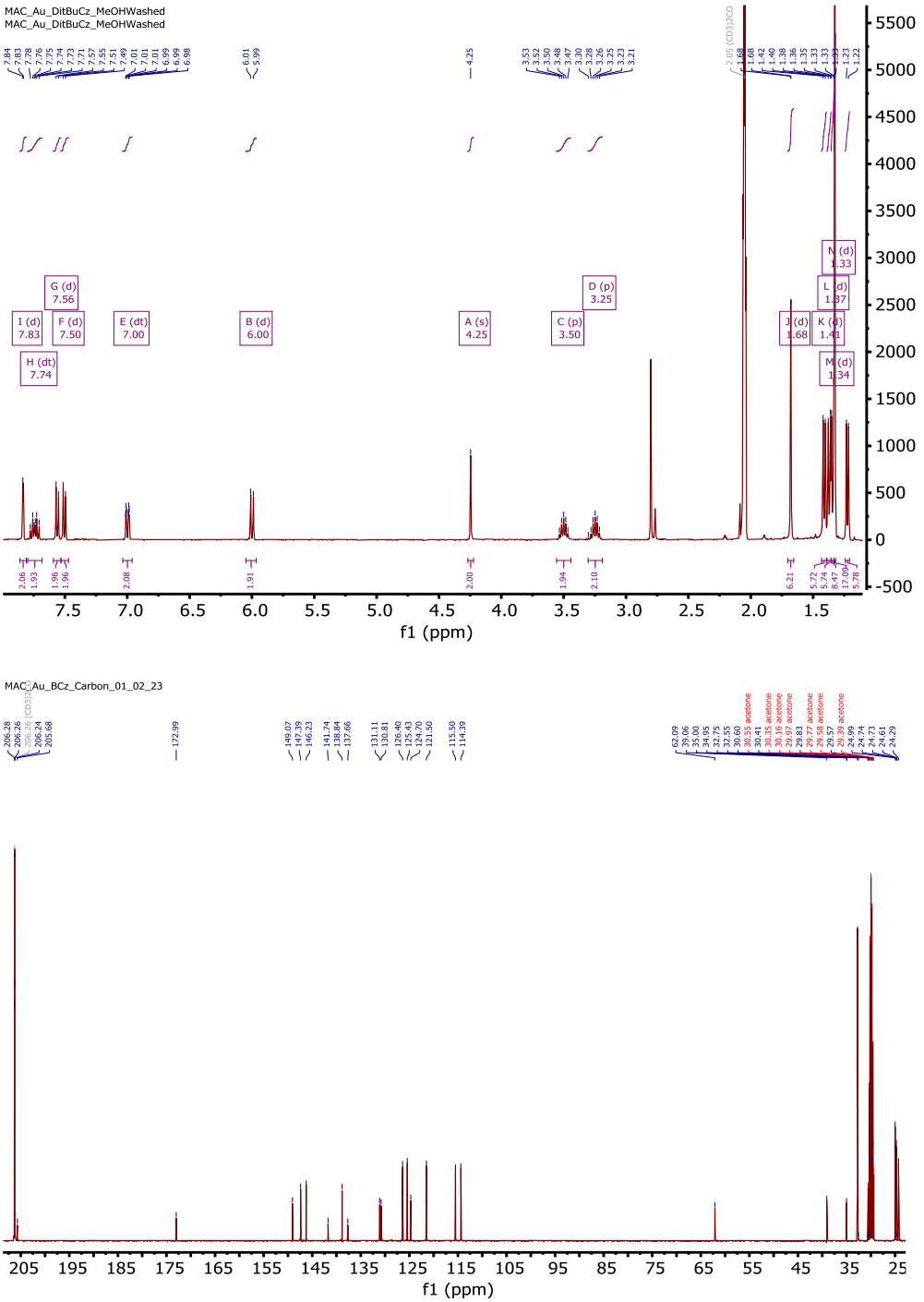

Figure S17. ^{1}H and ^{13}C NMR of Au_{BCz}^{MAC} in acetone-d6. The peaks at 2.05ppm and 2.8ppm in the ^{1}H NMR correspond to acetone and water respectively.